Theses and Dissertations

2018

Development and Verification of a Confined Discretized Solid Flame Model for Calculating Heat Flux on Concrete Tunnel Liners

Kyle James Root
Lehigh University, kjr216@lehigh.edu

Follow this and additional works at: https://preserve.lehigh.edu/etd

Part of the Structural Materials Commons

Development and Verification of a Confined Discretized Solid Flame Model for
Calculating Heat Flux on Concrete Tunnel Liners

by

Kyle Root

A Thesis

Presented to the Graduate and Research Committee

of Lehigh University

in Candidacy for the Degree of

Master of Science

in

Structural Engineering

Lehigh University

August 2018

This thesis is accepted and approved in partial fulfillment of the requirements for the Master of Science.

_____
Date

_____
Spencer E. Quiel
Thesis Advisor

_____
Clay J. Naito
Thesis Co-Advisor

_____
Panayiotis Diplas
Chairperson of Department
Civil and Environmental Engineering

ii

ACKNOWLEDGEMENTS

TABLE OF CONTENTS

LIST OF TABLES

TABLE OF FIGURES

viii

ABSTRACT

Road tunnels are susceptible to severe fire-induced heat flux due to the constant presence of vehicular traffic combined with the likelihood of accidents and subsequent combustion. Rapid assessment of thermal demands is a necessity to calculate appropriate design limit states and to better understand risk potential in a multitude of underground environments. A proposed approach is developed which allows for rapid assessment of thermal demands using models that are validated and informed through computationally intensive numerical assessment, experimental data, and semi-empirical relationships based on first principles. Utilizing Rhino and Grasshopper, the discretized solid flame model is adapted to account for the confinement present in tunnel structures and development of a convective zone under the tunnel ceiling. The confined discretized solid flame model (CDSF) accurately captures the spatial distribution of heat flux in circular tunnels as compared to experimentally-validated, high fidelity numerical solutions. Potential for cracking, spalling, breach, and other adverse structural consequences can be evaluated based on contour maps of total heat flux over the tunnel liner.

1

INTRODUCTION

Recent tunnel fires have highlighted the need for enhanced understanding of the structural response of the reinforced concrete liner to fire events. The St. Gotthard Tunnel fire of 2001 claimed the lives of 11 people and resulted in over 250 m of collapsed concrete lining within the tunnel. In 1999, the Mont Blanc Tunnel fire resulted in 39 casualties and over 900 m of damaged tunnel lining, with the blaze continuing for over 50 hours (Carvel 2004). As space above ground becomes limited, there is a concerted effort to move transportation infrastructure underground. A major example of this momentum is the 2016 establishment of the Boring Company in California, which aims to significantly increase the presence of underground transportation ("The Boring Company" n.d.).

Accurate and rapid assessment methods for tunnel systems would facilitate risk evaluation, retrofit design, suppression system deployment, and the potential development of new tunnel configurations. The array and inherent variability of inputs for a fire event calculation can be incorporated into a modified discretized solid flame (MDSF) model, which represents the flames and smoke as discretized solid objects with varying radiative power. The MDSF model was previously proposed by Quiel et al. (Quiel et al. 2015) for bridges exposed to open-air hydrocarbon fires - this method requires an "intermediate" level of computational effort between analytical calculations, semi-empirical models, and high-fidelity CFD solutions. Adapted from the MDSF, the new development of a confined discretized solid flame model (CDSF) which geometrically redefines the solid flame shape according to confinement and fire size while also including convective effects, is presented here.

2

To appropriately model a severe fire in a tunnel environment, the zone model and solid flame concepts are merged into a single approach that appropriately accounts for flame radiation, smoke effects, and convection from gaseous combustion byproducts. The CDSF is capable of providing rapid yet reliable predictions of the total heat flux received by tunnel liners from a range of typical vehicle design fires (Association 2011). Calibration of the CDSF model is performed via comparison to experimentally validated CFD solutions developed in NIST's publically available Fire Dynamics Simulator (FDS) (McGrattan et al. 2013). The computational efficiency of the CDSF model versus its CFD counterpart enables for stochastic assessment of numerous input parameters over an inventory of tunnels. A commercial 3D computer-aided design software, Rhinoceros 3D (Robert McNeel & Associates 2018b) and accompanied visual programming language, Grasshopper (Robert McNeel & Associates 2018a), are utilized to implement the CDSF model for their extended capabilities in complex, parametric geometric analysis and visualization.

BACKGROUND

To evaluate the resilience of tunnel liners to damage resulting from fire events, engineers must first calculate the fire-induced heat exposure and then determine the structural effects due to heat transfer. There are generally three types of fire models for thermal exposure evaluation: parametric standard fire curves, computational fluid dynamic (CFD) models, and empirical or semi-empirical models with varying complexity. In practice, a parametric fire curve is often used for its simplicity. A great deal of experimental work has been done to obtain time-temperature curves for potential types and sizes of fire in tunnels, among which the Rijkswaterstaat (RWS) time-temperature curve is one of the

3

most widely adopted standards worldwide. In the US, the National Fire Protection Association (NFPA) defines failure criteria and fire protection performance criteria for tunnels based on the RWS curve. The fire event is represented as an upper-bound temperature time history caused by combustion of a $50m^3$ fuel tanker with a heat release rate (HRR) of 300MW and duration of 120 min. The temperature rapidly increases to 1200°C in 10 minutes from ignition and remains above 1200°C for 2 hours (Association 2011). While the standard fire curve is easy to apply to the tunnel liner as a worst case, it does not consider spatial distribution of heat exposure, which results in overly conservative and inefficient designs. The use of a specified temperature time history circumvents the calculation of realistic heat transfer from the fire to the liner via flame radiation and convection from smoke and hot gases resulting from combustion.

CFD analyses provide high-resolution, data-rich calculations of fire demands within enclosures. However, these models require extensive computing time and a large amount of input, most of which must be assumed if experimental data or design guidance are not available. Such an approach is not feasible for rapid assessment of an inventory of tunnels and/or for a wide range of fire scenarios, nor is it practical for a stochastic assessment of structural resilience with realistically varying material and geotechnical characteristics of the tunnel. A model of intermediate complexity is therefore necessary for evaluation of numerous tunnel fire scenarios.

CDSF MODEL DESCRIPTION

The CDSF is a radiative and convective hybrid model for calculating incident heat flux on the surface of a tunnel liner. The flame is modelled as a discretized solid object with varied emissive power. Each target surface on the tunnel liner receives straight line

4

radiation from each discretized solid flame element. An approximate convective region, informed through computational modelling, is defined under the tunnel ceiling to account for additional thermal demands on the structure from developed ceiling jets. The summation of radiative and convective effects at each target surface is calculated and stored, Figure 1. Calculated, spatial distribution of heat fluxes on the tunnel liner can then be visualized directly on the tunnel structure and used for subsequent structural evaluation.
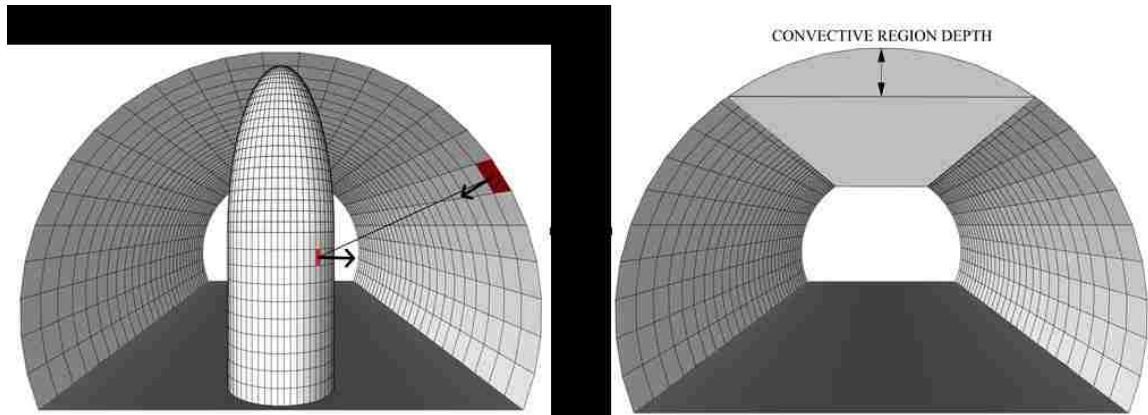
Figure 1 – Radiative and convective heat flux summation schematic

FDS has been integrated throughout the development of numerous aspects of the CDSF. The applicability of FDS in large scale tunnel fires has been previously established by members of the group (Root et al. 2018) through comparisons of temperature distribution obtained through FDS and full-scale, experimental data. While the use of FDS has been integral in the development of the model presented, it is not within the scope of this thesis and will be referenced without detailed description. Full description of the FDS model parameters used throughout the development can again be found in other work by the group (Root et al. 2018).

All geometric modelling and calculation is performed using Rhino and Grasshopper, thus allowing for continuous, analytical flame shapes and rapid visualization

www.manaraa.com

of thermal demands. While previous model iterations only addressed horseshoe-shaped cross sections (Root et al. 2018), the CDSF has been further refined to extend the range of capability to circular tunnels. Continued work will expand upon model parameters to capture all tunnel shapes and sizes.

The input parameters to the CDSF first require a fire size, defined through peak heat release rate (HRR) and geometric footprint. The model is generalized to accept footprints and HRR of varying size and shapes, however an approach for streamlining the input parameters has been developed. In recognition of the variability in vehicle material composition and contents, an equivalent diesel footprint is defined as a function of the HRR and initial vehicle footprint. The equivalent diesel footprint is calculated to achieve the same HRR as that specified for the vehicle type/size, while applying geometric constraints to ensure the footprint obeys a limiting aspect ratio. The aspect ratio is limited to 2.0 for the equivalent diesel footprint, where A_f (m^2) represents the area contained inside the rectangle. Because the semi-empirical relationships used are based on circular pools, research has indicated that using an effective diameter, $D_{f,eff}$ (Equation 1) for aspect ratios greater than 2.5 may lead to inaccuracies (McGrattan, Baum, and Hamins 2000).

$$D_{f,eff} = \sqrt{\frac{4A_f}{\pi}} \qquad (1)$$

Equation 2 shows the relationship between peak HRR, $\dot{Q}_{f,max}$ and the equivalent footprint of the pool fire (Babrauskas 2016) , where $D_{f,eff}$ is taken from Equation 1. Remaining equation parameters are fuel specific and are obtained from previous experimental work for diesel (Siddapureddy 2013); where $\dot{m}''$, $\Delta H_{c,eff}$ and $k\beta$ are mass

loss rate in *(kg/m²)*, effective heat of combustion in *(kJ/kg)* and an empirical constant in *(m⁻¹)*, respectively.

$$\dot{Q}_{f,max} = \dot{m}'' \Delta H_{c,eff} A_f (1 - e^{-k\beta * D_{f,eff}}) \tag{2}$$

Using Equations 1-2 for diesel specific combustion parameters, the rectangular, equivalent diesel footprint is iteratively solved for to equal the specified HRR, sample shown below in Figure 2 where the dashed and solid line represent the vehicle footprint and calculated, equivalent diesel footprint, respectively.

Figure 2 – Equivalent diesel footprint

The rectangular, equivalent diesel footprint is converted to an equivalent analytical elliptical footprint, to remove any discontinuities when the solid flame shape is extruded. An initial ellipse is inscribed in the rectangular footprint, then uniformly scaled in size to equate the perimeters of the rectangular and analytical shapes as detailed below in Figure 3, as the CDSF radiation is predicated on *surface* emissive power.

7
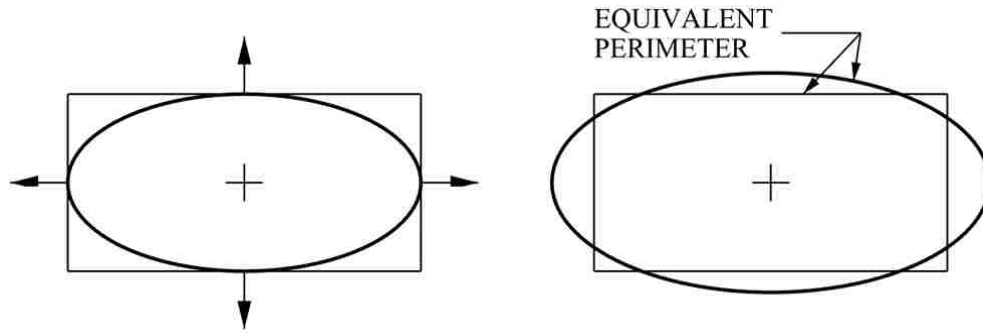
Figure 3 – Analytical elliptical footprint development

The progression of footprints, from vehicle to analytical elliptical can be seen below in Figure 4.
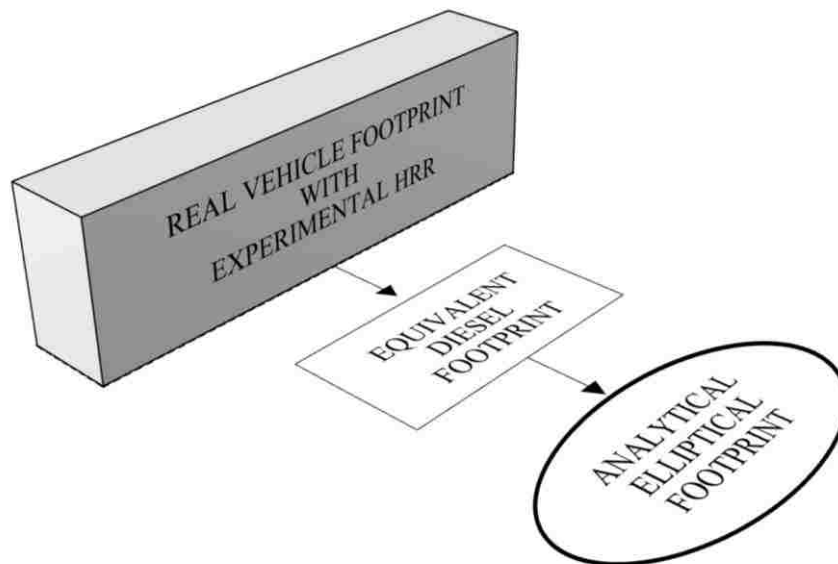
Figure 4 – Footprint development workflow

The solid flame shape generated without consideration of tunnel confinement is first calculated, represented as the free flame. If the free flame is determined to extend beyond the confines of the tunnel geometry and specified ceiling offset, the shape is compressed and becomes confined to the tunnel, regarded as the confined flame shape. The flame shape, either confined or free, is then appropriately discretized for analysis, denoted

8

as the analytical flame, for which varied emissive power is assigned to each discretized surface.

The height of the free flame H_f *(m)* is calculated as a function of the peak heat release rate, $\dot{Q}_{f,max}$ *(kW)* and effective diameter, $D_{f,eff}$, as specified in Heskestad's correlation (National Fire Protection Association 2016) Equation 3.

$$H_f = 0.235\dot{Q}_{f,max}^{0.4} - 1.02D_{f,eff} \tag{3}$$

The free flame is proportioned in accordance with work done by Zhou, in which the solid flame is bifurcated into an extruded ellipse body and cone at $0.4H_f$ from the base of the flame (Zhou et al. 2014). To again avoid discontinuities in the solid flame shape, the pointed cone shape is replaced with a truncated ellipsoid dome, evidenced in the illustrative graphic below in Figure 5.
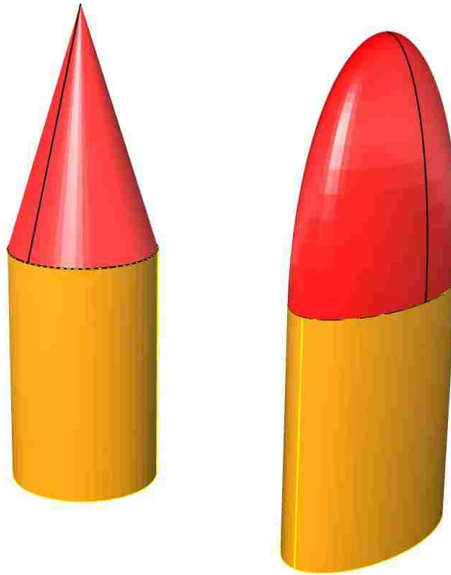
Figure 5 – Conical and elliptical flame shape comparison

This avoidance of sharp edges in the solid flame radiation calculation has been shown to produce more accurate accounting of heat flux received on the tunnel liner, especially at the tunnel ceiling in close proximity to the flame. The surface area of the free flame body and dome are represented as A_b (m^2) and A_d (m^2), respectively. The flame emissive power in (kW/m^2) is assumed to be uniform across the surface of the free flame, and calculated as a function of the radiative fraction, χ_r, peak heat release rate, and total free flame surface area A in (m^2), Equation 5, where radiative fraction is calculated in accordance with Equation 4 (Muñoz et al. 2007).

$$\chi_r = \begin{cases} 0.158D_{f,eff}{}^{0.15} \ for \ D_{f,eff} \leq 5m \\ 0.436D_{f,eff}{}^{-0.58} \ for \ D_{f,eff} > 5m \end{cases} \quad (4)$$

$$E = \frac{\chi_r \ \dot{Q}_{f,max}}{A} \quad (5)$$

As shown in Figure 6, the height of the fire's base above the road surface, H_{base} (m), approximately accounts for the height of the vehicle. If the height of the free flame H_f from Equation 3, originating from H_{base} above the road surface, remains below the tunnel height minus a specified ceiling offset of $0.02H_f$, then H_f is used as the analytical flame height. However, the free flame height from Equation 3 will often exceed the height of the tunnel minus the ceiling offset for significant fires. In those cases, the analytical flame height is reduced to fit inside the tunnel enclosure, thus *confined*.

10
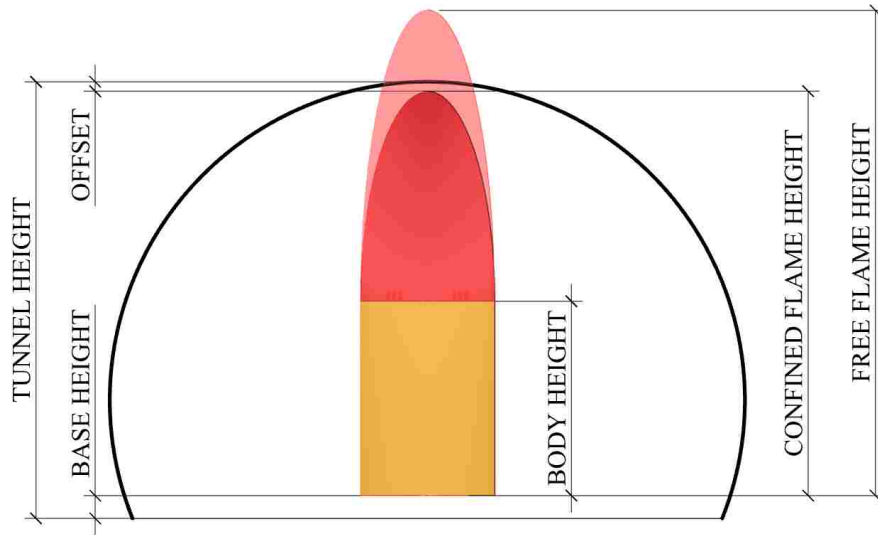
Figure 6 - Schematic comparison of the free flame and confined flame shapes

To allow the flame surfaces to have adequate view of the tunnel liner at close range and "engulf" those targets with appropriately high radiation heat flux, the top of the ellipsoid dome is restricted to an offset of $0.02H_f$ from the tunnel ceiling height. The confined flame height, H_c, (m) is therefore calculated as follows.

$$H_c = H_T - 0.02H_f - H_{base} \tag{6}$$

For free flame heights that just exceed the tunnel height, the dome is simply compressed as shown in Figure 6 while the height of the extruded ellipse body remains as $0.4H_f$. As the free flame height increases for increasingly severe fires, the body height can become so large that the ellipsoid dome would be unrealistically compressed or even eliminated (resulting in poor analytical calculations of radiation heat flux on the ceiling) if no height adjustments were made to the body. To preserve the bifurcated structure of the confined solid flame, the height of the confined flame body can be no greater than 75% of H_c, and the ellipsoid dome can therefore be no less than 25% of H_c. Note that because H_c

is itself a function of the free flame height, confined flame heights will actually reduce further below the tunnel ceiling with fires of increasing severity, thus accounting for the additional flame spread and pluming around the fire's center expected with increasing fire size.

Conservation of energy is preserved when free flame shapes that extend beyond the tunnel height are compressed to create the confined flame shape, which will naturally have less surface area. Since the ellipsoid dome and extruded ellipse body will experience different amounts of surface area reduction, the average emissive power over the free flame surface area, E in (kW/m^2) from Equation 5 is increased by the ratios shown below in Equation 7 and Equation 8 for the body and dome of the confined flame, respectively.

$$E_b = E\left(\frac{A_b}{A_b{'}}\right) * C \tag{7}$$

$$E_d = E\left(\frac{A_d}{A_d{'}}\right) * C \tag{8}$$

A_b and A_d (both in m^2) are the areas of the free flame body and dome, and $A_b{'}$ and $A_d{'}$ (again in m^2) are the areas of the confined flame body and dome, respectively. Surface emissive power in the body, E_b (kW/m^2) and surface emissive power in the dome, E_d (kW/m^2), are applied to the analytical flame body and dome, respectively. Additionally, when the free flame height far exceeds the tunnel height and the body height is restricted to 75% of H_c, the average emissive power, E, is increased by an additional confinement factor, C, to account for increased combustion efficiency and turbulence resulting from significant confinement of the flame (Wang et al. 2017). At present, C is taken as the ratio of A_b to $A_b{'}$. Note this value equals unity for free flame body heights not exceeding 75%

12

of H_c. As will be demonstrated, this approach to energy conservation between the free and confined solid flame models can accurately capture the magnitude and distribution of radiation heat fluxes expected with increasing fire size as compared to the FDS solutions. Preliminary study has indicated a maximum edge distance of 85 cm in the analytical flame mesh provides an acceptable level of resolution and convergence. Future model development will further investigate the trade-off between analysis time and slight variation in the calculated heat flux from radiation.

With analytical flame shape and surface emissive powers defined, the radiative heat flux contribution can be calculated. Radiative contribution from each emitting surface, *i*, is summed at each target surface, *j*. Incident heat flux at each discretized surface, q''_j is calculated as a function of the emissive power and view factor, $F_{i \to j}$ between receiving and emitting surfaces as shown below in Equation 9.

$$q''_j = \sum_{i=1}^{n} E_i F_{i \to j} = \sum_{i=1}^{n} E_i \frac{A_i \cos \theta_i \cos \theta_j}{\pi r_{i \to j}^2} \tag{9}$$

The addition of a convective field at the tunnel ceiling is provided in the CDSF to conservatively capture ceiling jet effects. Previous iterations of the model neglecting the effects of a connective zone under the tunnel ceiling were unable to accurately capture the longitudinal spread of thermal demands. Through FDS-informed calibration, additional convective heat flux is applied to target elements within the defined convective zone, having a depth denoted as D_{CZ} in *(m)*.

13
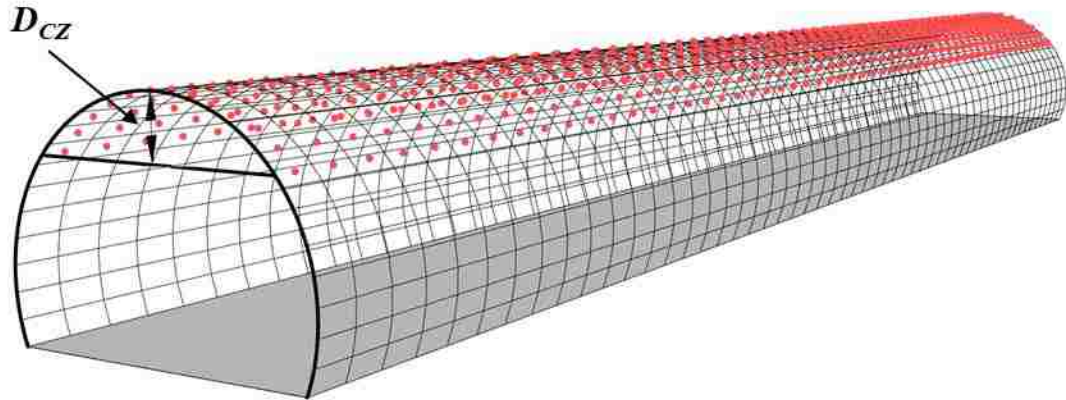
Figure 7 – Depth of convective zone under tunnel ceiling

The depth of the convective zone below the tunnel ceiling is calculated as a percentage of H_T, where D_{CZ}/H_T has been found to have the following correlation illustrated below in Figure 8 and detailed in Equation 10. Note this correlation has only been made for fire sizes between 30MW and 200MW. Additional analysis and comparisons should be performed before extending the application of the convective depth calibration to fire sizes outside of this range.
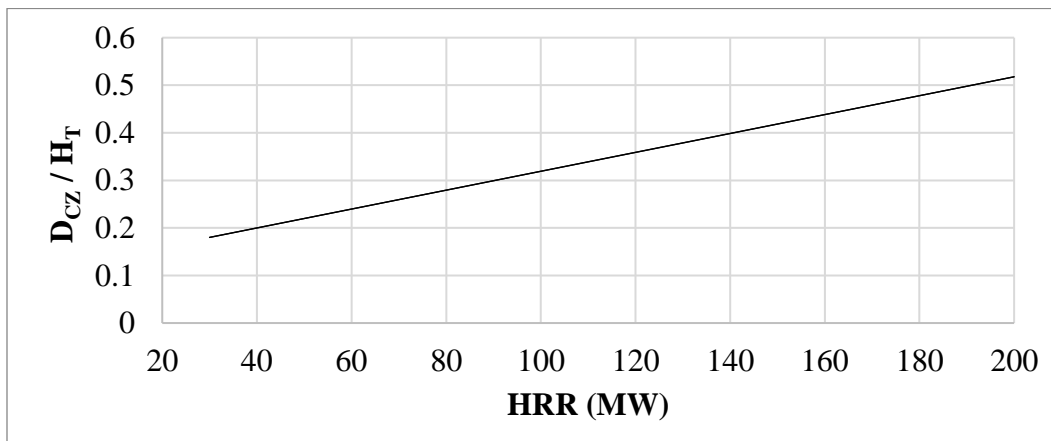
Figure 8 – Depth of convective zone calibration

$$\frac{D_{CZ}}{H_T} = 0.002\,(HRR) + 0.1204 \tag{10}$$

Kurioka et al. determined a power scaling fit for longitudinal temperature decay in the smoke filled region accumulating under a tunnel ceiling (Kurioka et al. 2003). Using an FDS-informed fit correlated to peak heat release rate and tunnel size, a similar model has been developed for the longitudinal decay of convective heat flux under the tunnel ceiling. A maximum convective heat flux is first defined with the fit determined below in Figure 9 and detailed in Equation 11.
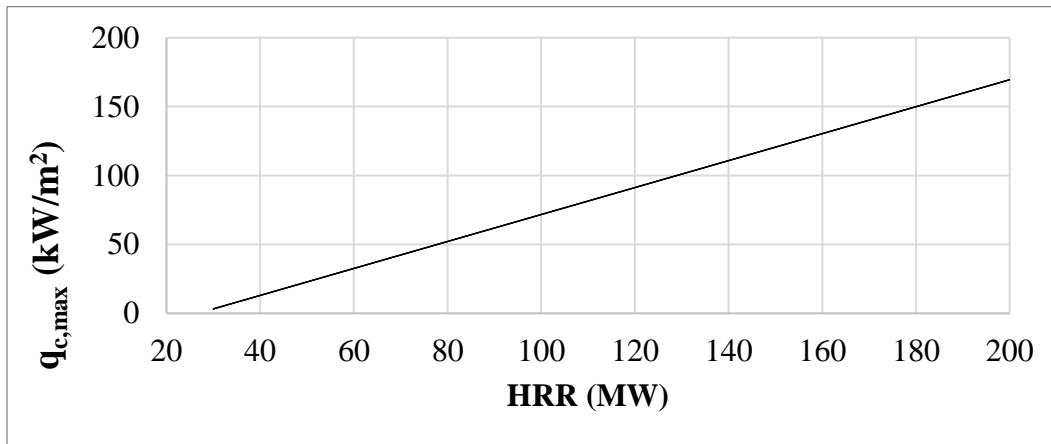
Figure 9 – Maximum convective heat flux calibration

$$q_{c,max} = 0.9788\,(HRR) - 26.118 \tag{11}$$

15

The longitudinal scaling from $q_{c,max}$ is detailed in Equations 12-14 below, where x in *(m)*, represents the longitudinal distance from the fire center.

$$\frac{q_c}{q_{c,max}} = \alpha \left(\frac{x}{H_T}\right)^{\beta} \tag{12}$$

$$x_0 = 0.26\dot{Q}_{f,max}^{0.2} \tag{13}$$

$$\frac{x}{H_T} \leq x_0, \ \alpha = 1, \ \beta = 0 \tag{14}$$
$$\frac{x}{H_T} > x_0, \ \alpha = 0.09\dot{Q}_{f,max}^{0.4}, \ \beta = -2.8\dot{Q}_{f,max}^{-0.2}$$

This longitudinal scaling from maximum convective heat flux is illustrated below for a range of HRR, note the horizontal axis denotes the value x in *(m)*, and the vertical axis represents maximum convective heat flux at that longitudinal distance, q_c in (*kW/m²*). The correlated scaling has proven to accurately capture the longitudinal spread and magnitude of large scale fires ranging from 30MW to 200MW.

16
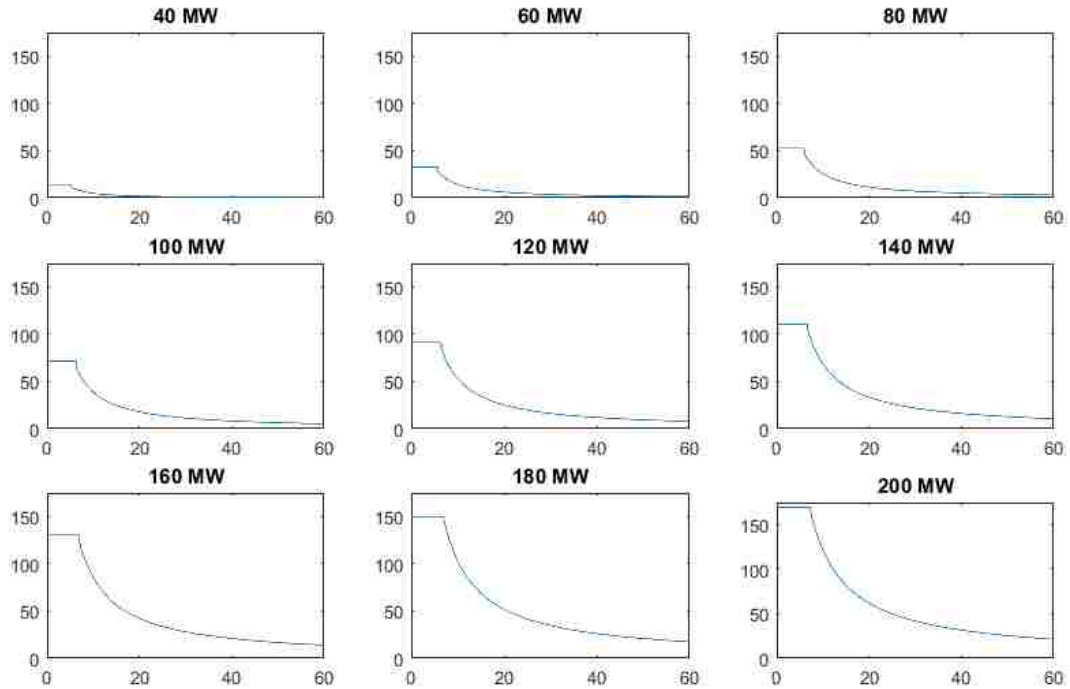
Figure 10 – Longitudinal scaling of maximum applied convective heat flux

The convective heat flux is further scaled linearly through the depth of the convective zone, as informed by Hu (Hu et al. 2004), who noted a strong correlation between smoke temperature and distance below tunnel ceiling. A sample convective zone noting applied q_c in (kW/m^2) is shown below for a 70MW fire, Figure 11.

17
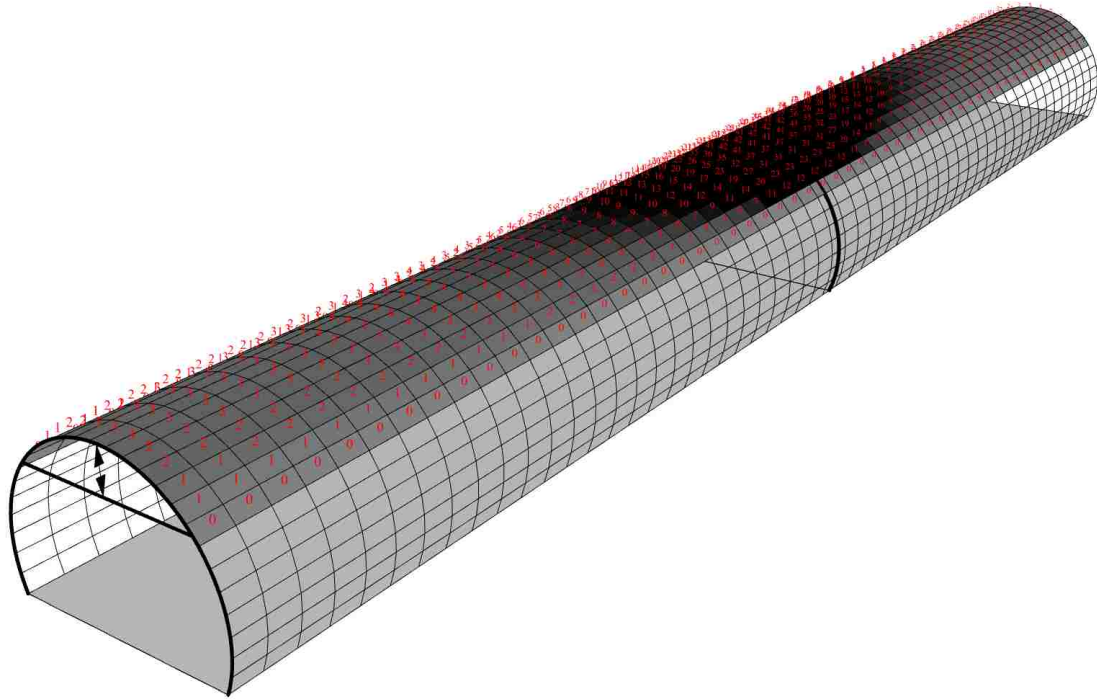
Figure 11 – 70 MW convective heat flux distribution

The correlations presented for additional heat flux applied within the convective zone have been determined for fire sizes ranging from 30MW to 200MW in a circular tunnel. Work done by others notes the dependency on tunnel ceiling shape to the heat accumulation under the ceiling, even with equal cross-sectional area (Kurioka et al. 2003). Preliminary analysis suggests the applicability of these correlations to horseshoe-shaped cross sections, however future work will consider generalizing the approach to accurately capture differing heat accumulation under tunnels with flat ceilings. Combining radiative and convective effects at each tunnel element yields a total mapping of incident heat flux in (kW/m^2) on the tunnel liner, as shown below in Figure 12. The full workflow in Grasshopper can be seen illustrated in Appendix 1: CDSF Grasshopper Workflow.
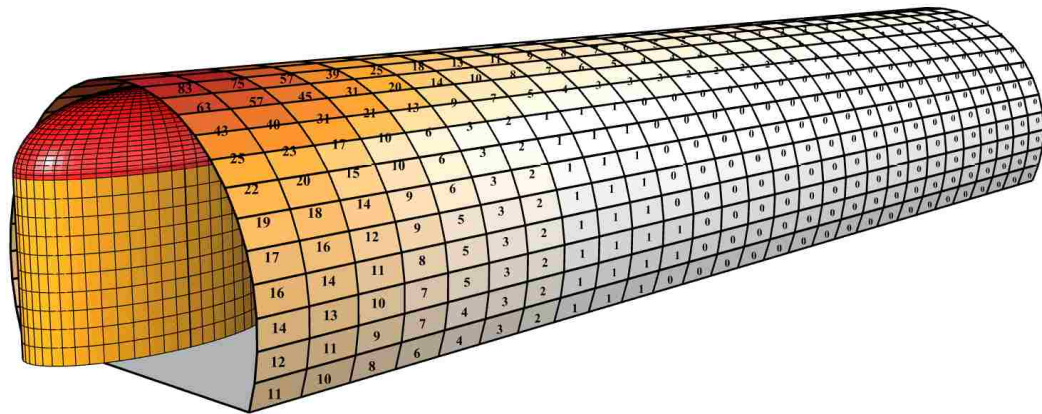
Figure 12 – Heat flux distribution on cross section at longitudinal center of tunnel

ILLUSTRATIVE EXAMPLE AND MODEL VERIFICATION

To demonstrate the application of the CDSF in a manner which allows for complete visualization of the process, an illustrative example is carried out below. A tunnel cross section must first be selected. The circular tunnel chosen here is representative of a real tunnel in service, dimensions shown below in Figure 13.
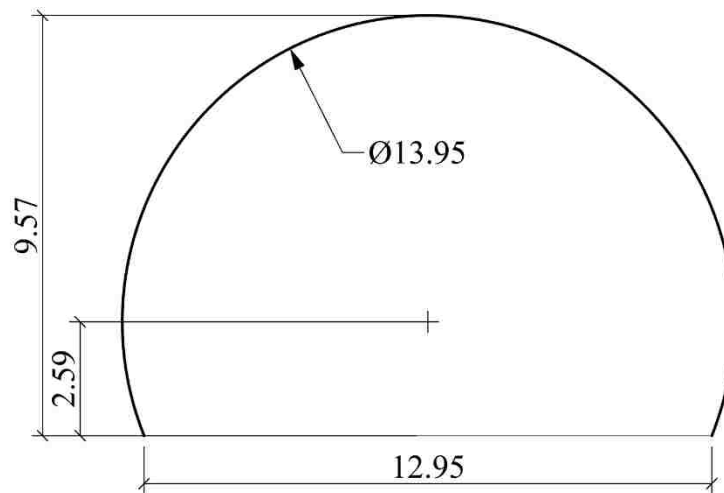
Figure 13 – Circular tunnel dimensions

19

The tunnel cross section is extruded in the longitudinal direction to the desired analysis length and meshed. A total analysis length of 110 meters is selected here. For illustrative purposes, the tunnel walls have been crudely discretized for simplification during the verification process, with 10 elements along both the longitudinal and circumferential axes. The tunnel analysis mesh with 100 total faces is shown below in Figure 14.
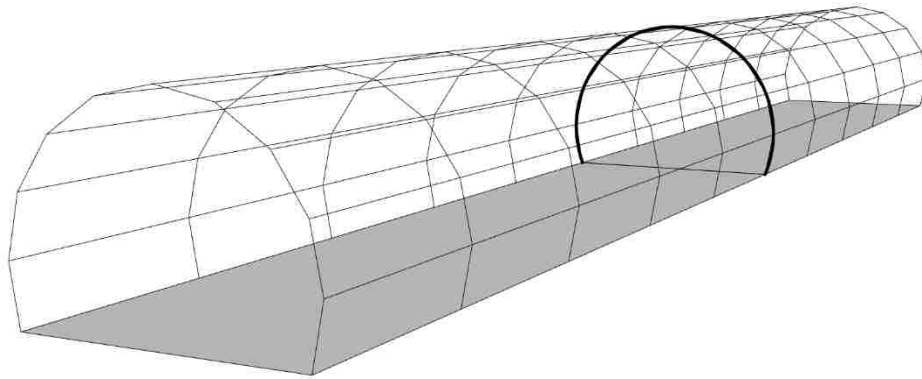
Figure 14 – Tunnel mesh coarse discretization

With the tunnel analysis mesh defined, the fire must next be defined. A 70 MW fire is selected here as representative of a light heavy goods vehicle (HGV) (Association 2011). Dimensions of the HGV as illustrated in Figure 15, are taken from vehicle WB-12 in AASHTO design guidance (American Association of State Highway and Transportation Officials 2001).

20
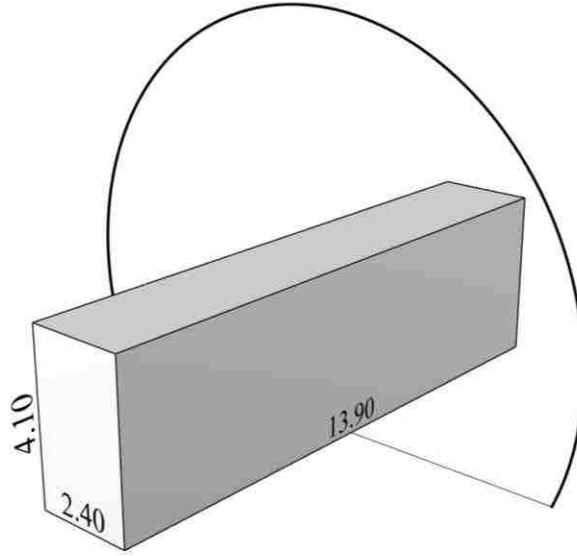
Figure 15 – Light HGV vehicle dimensions in tunnel cross section

First, the aspect ratio, A_r of the vehicle footprint is calculated as the ratio of the long edge, L_f *(m)* to the short edge, W_f *(m)*.

$$A_r = \frac{L_f}{W_f} = \frac{13.90\ m}{2.40\ m} = 5.79$$

Limiting the aspect ratio to 2.0 to remain within the acceptable range of the semi-empirical formula for flame height (Equation 3), the equivalent rectangular diesel footprint is iteratively calculated to satisfy the relationship between effective diameter $D_{f,eff}$ (Equation 1) and peak HRR, $\dot{Q}_{f,max}$. Combustion parameters are obtained from previous experimental work for diesel (Siddapureddy 2013); where mass loss rate, $\dot{m}''$ is 0.057 kg/m^2-s, heat of combustion, $\Delta H_{c,eff}$ is 47,000 *kJ/kg* and $k\beta$ is an empirical constant equaled to 1.16 m^{-1}. Results of the iterative calculation are shown satisfied for the conditions below, yielding the equivalent rectangular footprint with dimensions 7.23 *m* by 3.62 *m*.

21

$$\dot{Q}_{f,max} = \dot{m}'' \Delta H_{c,eff} A_f \left(1 - e^{-k\beta * D_{f,eff}}\right)$$

$$0.057 \frac{kg}{m^2 s} * 47{,}000 \frac{kJ}{kg} * 26.2 m^2 \left(1 - e^{-1.16 m^{-1} * 5.77 m}\right) = 70 MW$$

Comparison between vehicle footprint, dashed, and the calculated, equivalent diesel footprint, solid, is shown below in Figure 16.
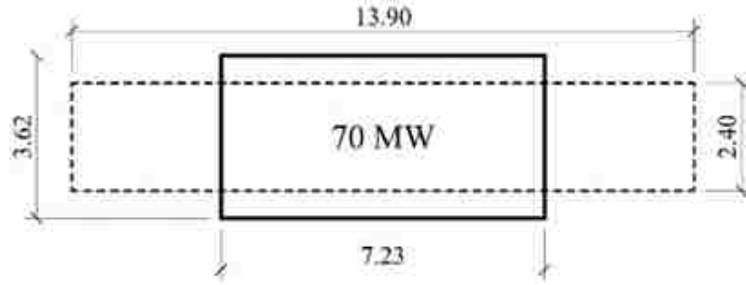
Figure 16 – Vehicle footprint and equivalent deisel footprint dimensioned (*m*)

Radiative fraction is calculated in accordance with Equation 4, for the case in which diameter is larger than 5 *m* as $D_{f,eff}$ has been calculated as 5.77 *m*. Important to note, is that $D_{f,eff}$ is used in the calculation of radiative fraction.

$$\chi_r = 0.436 D^{-0.58} = 0.158$$

Discontinuities in the subsequent solid flame shape are now removed by converting the equivalent diesel footprint into the analytical, elliptical footprint. An initial ellipse is first inscribed in the equivalent diesel footprint. However, because the solid flame model is predicated on surface emissive power, the ellipse is uniformly scaled to achieve the same perimeter as that of the equivalent diesel footprint. Final dimensions of the elliptical footprint are shown in Figure 17.

22
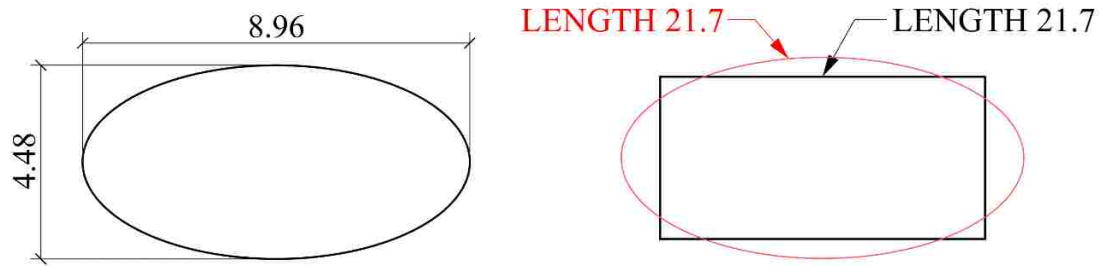
Figure 17 – Analytical elliptical footprint (*m*)

Free flame height in *(m)*, independent of tunnel confinement, can then be determined through Heskestad's semi-empirical correlation (Equation 3).

$$H_f = 0.235 * (70MW)^{0.4} - 1.02 * (5.77m) = 14.49m$$

The free flame is portioned into the body and dome at a height of $0.4H_f$.

$$0.4H_f = 0.4(14.49m) = 5.80m$$

The flame is assumed to act 1 *m* above the road surface to account for vehicle height, H_{base} equalled to 1 *m*, illustrated below in Figure 18.

23
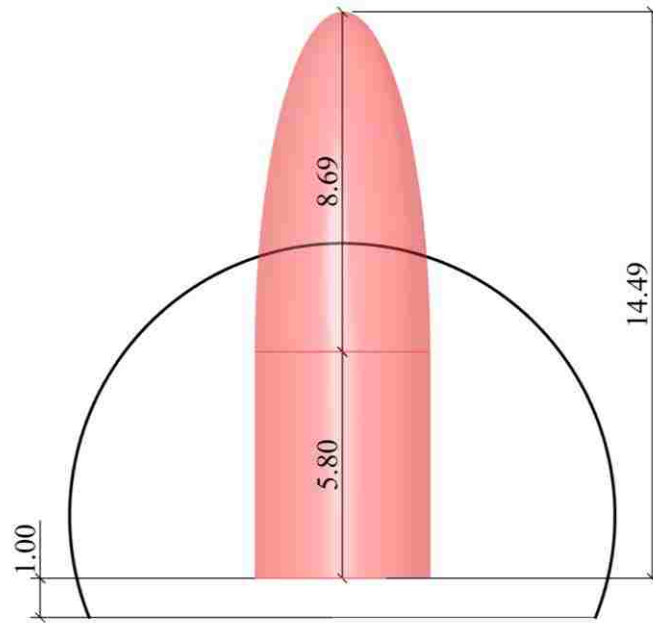
Figure 18 – Dimesioned free flame in tunnel cross section (*m*)

The surface areas of the free flame body, A_b and dome, A_d are geometrically calculated in the workflow as 125.8 *m²* and 154.9 *m²*, for a total free flame area, *A* of 280.7 *m²*. Average surface emissive power can be determined through Equation 5 as shown below.

$$E = \frac{0.158*70E3kW}{280.7m^2} = 39.34\frac{kW}{m^2}$$

Because the calculated free flame clearly extends above the limiting elevation, tunnel confinement is now taken into account by reducing the flame height and thus generating the new, confined flame. As stated in Equation 6, the confined flame height is calculated as follows, where the height of the tunnel, H_T can be seen in the dimensioned cross section in Figure 13 as 9.57 *m.* The confined flame dome extends up to the specified offset from the tunnel ceiling, calculated as 2% of the free flame height.

24

$$offset = 0.02(14.49\text{m}) = 0.290m$$

The height of the confined flame body is set to 75% of the confined flame height in the tunnel.

$$H_c = H_T - offset - H_{base} = 9.57\text{m} - 0.290\text{m} - 1\text{m} = 8.28\text{m}$$

$$0.75H_c = 0.75(8.28\text{m}) = 6.21\text{m}$$

Therefore, because the height of the body in the free flame, 5.80 m, is less than 75% of the confined flame height, the height of the body in the confined flame is maintained as the height of body in the free flame. The dimensioned confined flame can be seen below in Figure 19.

Figure 19 – Dimesnioned confined flame (m)

With the confined flame shape defined, it can now be carried through to analysis, thus becoming the analytical flame. Emissive power in the body and dome of the analytical flame are next calculated. The confining factor C is taken as unity here as A_b is equal to
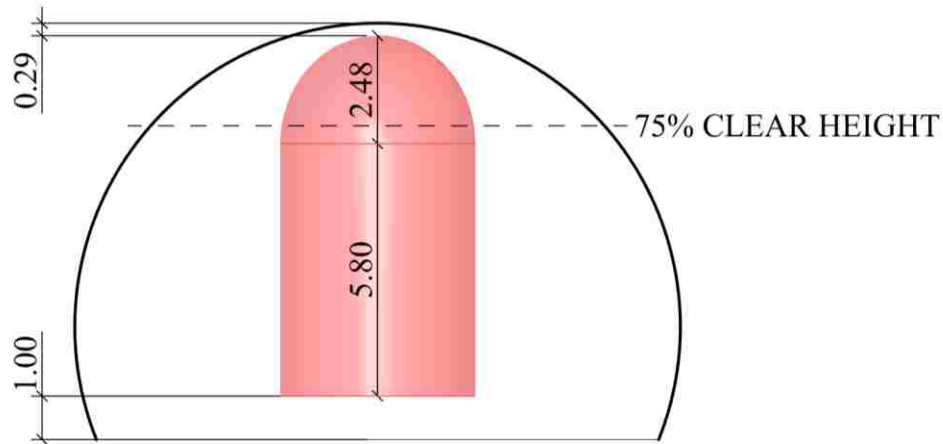
25

A_b' when the free flame body is not geometrically reduced. Surface areas of the analytical body, A_b' in *(m²)* and dome, A_d' in *(m²)* are again built into the workflow and calculated as 125.8 *m²* and 57.24 *m²*, respectively. Utilizing the expressions outlined in Equation 7 and Equation 8 to increase emissive power in the body and dome, the following values are determined.

$$E_b = 39.34 \frac{kW}{m^2} \left(\frac{125.8m^2}{125.8m^2} \right) * 1.0 = 39.34 \frac{kW}{m^2}$$

$$E_d = 39.34 \frac{kW}{m^2} \left(\frac{154.9m^2}{57.24m^2} \right) * 1.0 = 106.4 \frac{kW}{m^2}$$

With varied emissive power acting over the analytical flame, the radiative effects from each, discretized fire surface can now be calculated and summed at every target surface on the tunnel liner. The analytical flame mesh selected for this illustrative example is extremely coarse, with only 12 elements in the body and 8 elements in the dome. The discretization in the flame used is purely for demonstrative purposes, and it must be noted that a flame mesh with so few elements is not recommended for calculation. Preliminary study has indicated a maximum edge distance of 85 cm in the analytical flame mesh provides an acceptable level of resolution and convergence. Future studies will further investigate the trade-off between analysis time and slight variation in the calculated heat flux from radiation. A comparison between mesh size used for this example, 20 elements, relative to the typical mesh size used in analysis, 1890 elements, can be seen below in Figure 20.
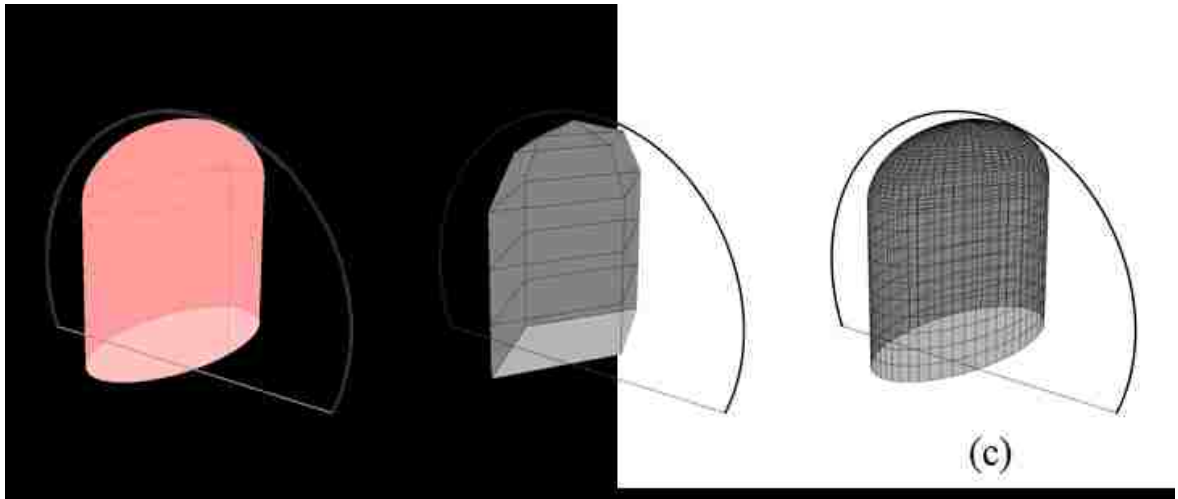
Figure 20 – Analytical solid flame (a) coarse mesh (b) and typical analytical mesh (c)

Normal vectors at each flame center and each target surface can be visualized to verify appropriate sense of the vectors before calculation of the view factors, Figure 21 and Figure 22, below. More specifically, flame normal vectors should be pointed out toward the tunnel mesh, and target normal vectors pointed in toward the flame mesh.
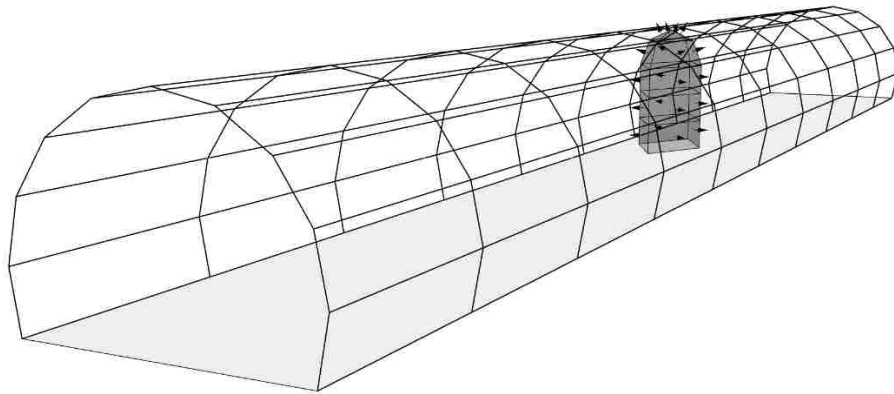
Figure 21 – Flame mesh normal vectors
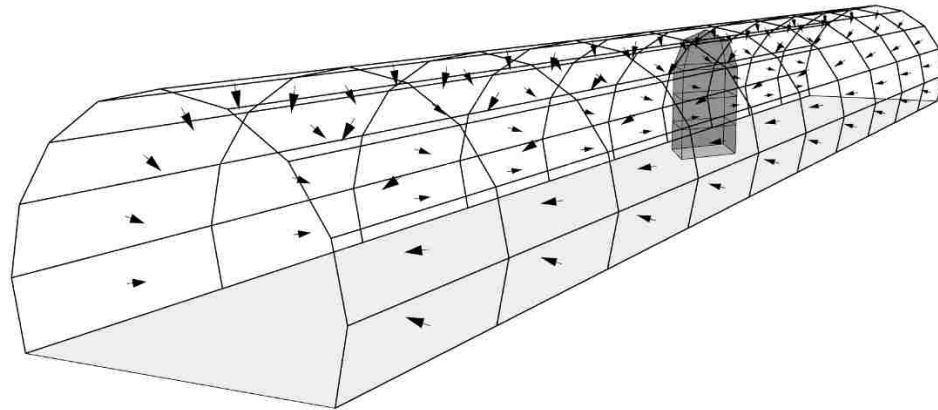
Figure 22 – Tunnel mesh normal vectors

For this example, two target surfaces are selected – one close to the road surface 16.5 *m* in the longitudinal direction from the center of fire source, tunnel mesh element number 30, and one near the tunnel ceiling 5.5 *m* in the longitudinal direction from the center of the fire source, tunnel mesh element number 54 shown below in Figure 23.
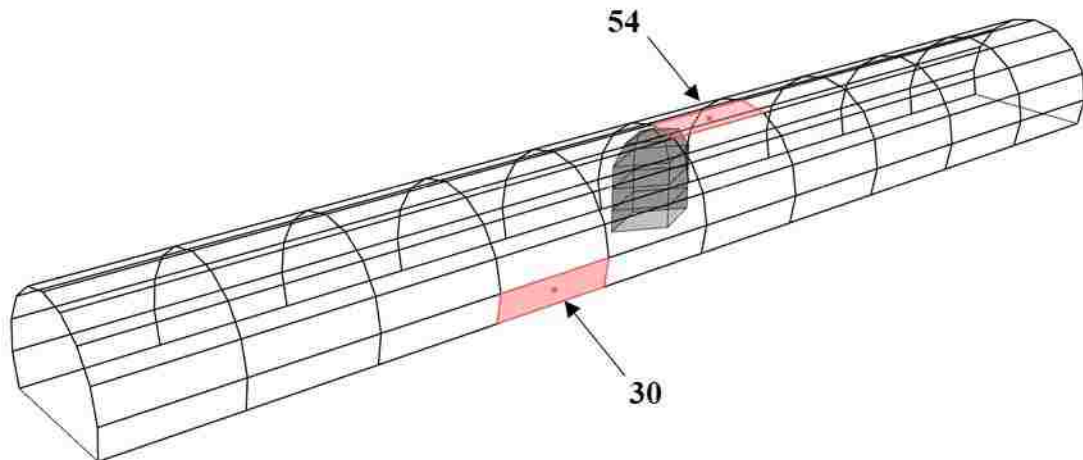
Figure 23 – Selected tunnel mesh elements

Originating from the center of each target element, *j*, chords are defined to the centers of each of flame mesh element, *i*. A total of n_i x n_j chords are defined, where n_i

and n_j represent the number of elements in the flame mesh and tunnel mesh, respectively. The relative angle between the chord connecting a given target center to flame center, and normal vector at that flame element is defined as θ_i in *(degrees)*, and the relative angle between the same chord and normal vector at each target element is defined as θ_j in *(degrees)*. The length of the chord is measured as $r_{i \to j}$ in *(m)*, and the surface area of the flame mesh face is additionally calculated and stored as A_i in *(m²)*. The summation of energy on each flame element received at tunnel mesh element number 30 can be seen below in Figure 24.
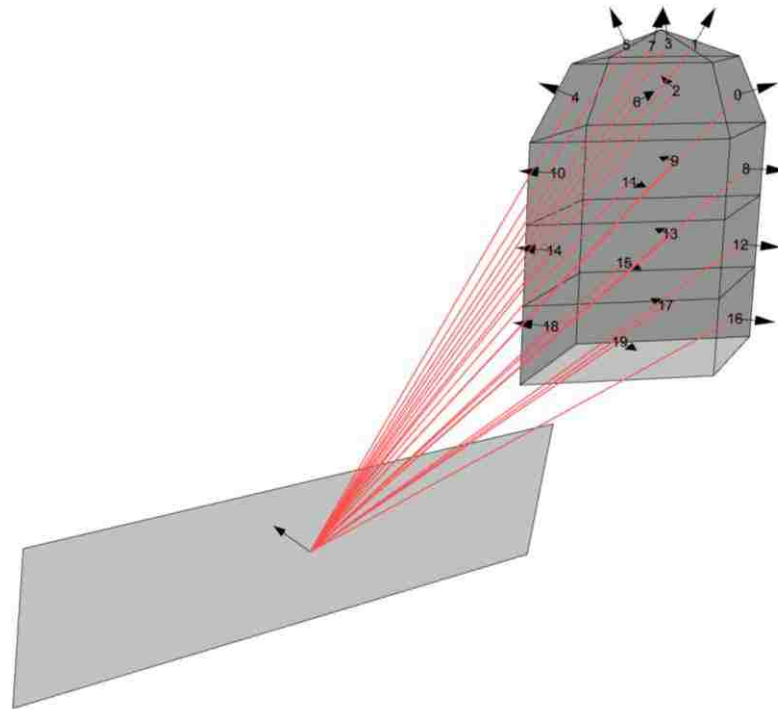
Figure 24 – Chords beween tunnel mesh element number 30 and flame mesh elements

In the given flame discretization, only a few elements have the radiation angles necessary for the selected target surface to receive radiation. More specifically, when the product of the cosines of angles θ_i and θ_j is less than or equal to 0, the view factor is set to 0, as the

flame element is "unable to see" the target surface in the orientation. The summation of

energy is tabulated for tunnel mesh element number 30 below in Table 1.

Table 1 – Summation of radiative energy for tunnel mesh element number 30

|	INDEX	E_i $\left(\frac{kW}{m^2}\right)$	A_i (m^2)	θ_i	θ_j	$r_{i \to j}$ (m)	$F_{i \to j}$	$E_i F_{i \to j}$ $\left(\frac{kW}{m^2}\right)$
DOME	0	106.439	7.911	104.044	70.321	20.311	0.000	0.000
	1	106.439	2.821	112.728	67.506	19.915	0.000	0.000
	2	106.439	7.911	141.3	65.385	20.935	0.000	0.000
	3	106.439	2.821	130.79	65.409	20.18	0.000	0.000
	4	106.439	7.911	97.616	60.422	17.665	0.000	0.000
	5	106.439	2.821	110.017	63.53	18.841	0.000	0.000
	6	106.439	7.911	57.595	66.158	16.921	0.002	0.203
	7	106.439	2.821	92.964	65.757	18.556	0.000	0.000
BODY	8	39.337	9.678	99.661	71.59	20.072	0.000	0.000
	9	39.337	9.678	137.734	65.767	20.809	0.000	0.000
	10	39.337	9.678	92.171	59.615	16.886	0.000	0.000
	11	39.337	9.678	44.493	66.612	15.969	0.003	0.135
	12	39.337	9.678	99.831	72.347	19.729	0.000	0.000
	13	39.337	9.678	138.763	66.441	20.478	0.000	0.000
	14	39.337	9.678	92.225	60.214	16.477	0.000	0.000
	15	39.337	9.678	42.842	67.35	15.536	0.004	0.142
	16	39.337	9.678	99.911	73.292	19.571	0.000	0.000
	17	39.337	9.678	139.253	67.346	20.327	0.000	0.000
	18	39.337	9.678	92.251	61.272	16.288	0.000	0.000
	19	39.337	9.678	42.027	68.475	15.335	0.004	0.140
							Σ	0.620

Flame elements with non-zero view factors are highlighted below in Figure 25 and can be additionally verified for corresponding indexing, angles, curve lengths, and flame surface areas as compared to those tabulated above.
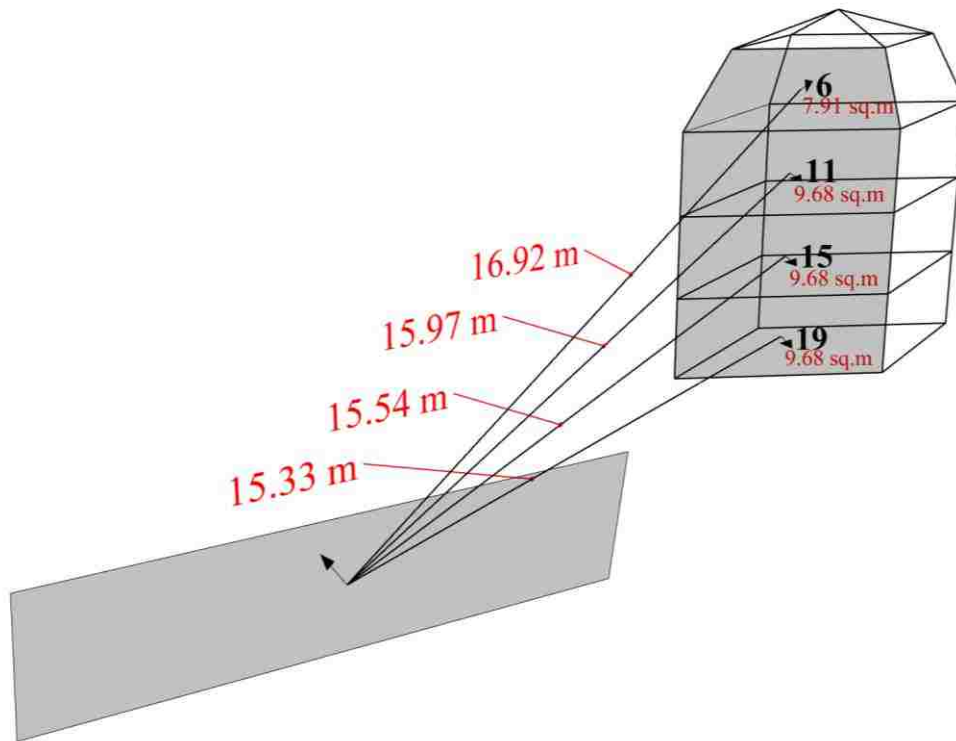
Figure 25 – Chords connecting tunnel mesh element number 30 to flame mesh elements having non-zero view factor

Additional verification is provided at tunnel mesh element 54, illustrated in Figure 23. Chords between the tunnel mesh element center and flame element centers with non-zero view factors can be seen below in Figure 26.

31
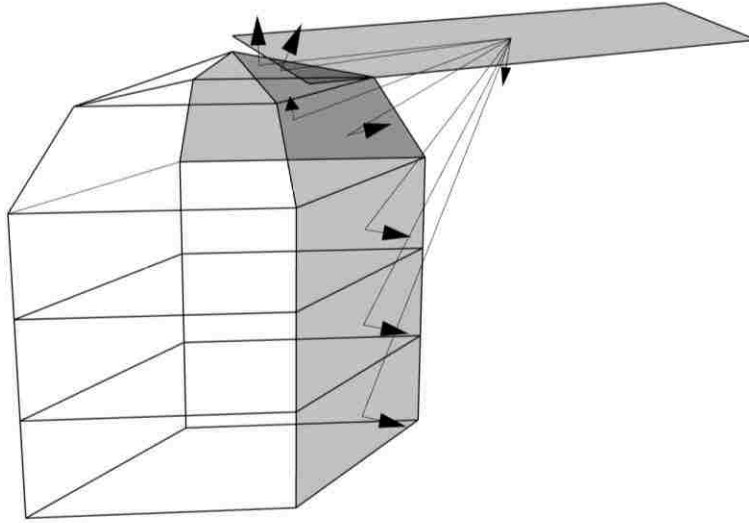
Figure 26 - Chords connecting tunnel mesh element number 54 to flame mesh elements
having non-zero view factor

The corresponding tabulated summation of radiation received at tunnel mesh element number 54 can be seen below in Table 2. As is expected, the flame elements in the dome contribute significantly to the radiative energy received by the tunnel element because of the increased emissive power, comparatively small radiative angles, and short standoff distances.

Table 2 - Summation of radiative energy for tunnel mesh element number 54

	INDEX	E_i $\left(\frac{kW}{m^2}\right)$	A_i (m^2)	θ_i	θ_j	$r_{i \to j}$ (m)	$F_{i \to j}$	$E_i F_{i \to j}$ $\left(\frac{kW}{m^2}\right)$
DOME	0	106.439	7.911	53.518	65.012	3.959	0.040	4.295
	1	106.439	2.821	69.472	83.274	4.815	0.002	0.169
	2	106.439	7.911	88.706	63.349	4.555	0.001	0.131
	3	106.439	2.821	83.085	81.796	5.028	0.001	0.065
	4	106.439	7.911	125.149	75.062	7.926	0.000	0.000
	5	106.439	2.821	104.528	83.697	6.535	0.000	0.000
	6	106.439	7.911	107.714	77.287	7.599	0.000	0.000
	7	106.439	2.821	95.009	84.923	6.373	0.000	0.000
BODY	8	39.337	9.678	69.851	43.683	4.769	0.034	1.327
	9	39.337	9.678	97.843	43.532	5.356	0.000	0.000
	10	39.337	9.678	129.787	63.913	8.830	0.000	0.000
	11	39.337	9.678	112.716	66.026	8.487	0.000	0.000
	12	39.337	9.678	74.927	32.219	6.316	0.017	0.668
	13	39.337	9.678	96.197	31.415	6.771	0.000	0.000
	14	39.337	9.678	125.406	53.671	9.753	0.000	0.000
	15	39.337	9.678	110.306	55.539	9.444	0.000	0.000
	16	39.337	9.678	78.200	25.679	8.032	0.009	0.346
	17	39.337	9.678	94.995	23.917	8.394	0.000	0.000
	18	39.337	9.678	121.090	45.477	10.943	0.000	0.000
	19	39.337	9.678	107.892	47.269	10.668	0.000	0.000
							Σ	7.002

Looking at the typical CDSF output for radiation only, the values calculated above can be verified once more as shown in Figure 27, highlighting the heat flux in (kW/m^2) for tunnel mesh elements number 30 and number 54.
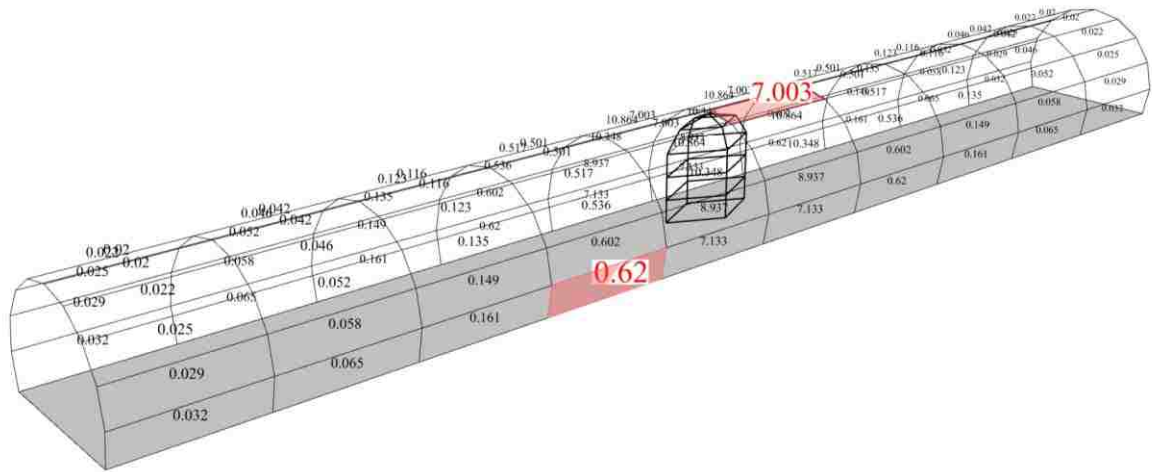
Figure 27 – Radiative heat flux output highlighting selected tunnel mesh elements

With the radiative component of the CDSF verified, the illustrative example will be extended to include the additional convective heat flux imparted on the target elements within the defined convective zone. The depth of the convective zone is first determined per the empirical correlation provided in Figure 8 and Equation 10.

$$\frac{D_{CZ}}{H_T} = 0.002(70MW) + 0.1204 = 0.260$$

For the tunnel height, H_T of 9.57 m, the depth of the convective zone is calculated as 2.49 m. Target elements with an elevation greater than or equal to $H_T - D_{CZ}$ are shown below in Figure 28.
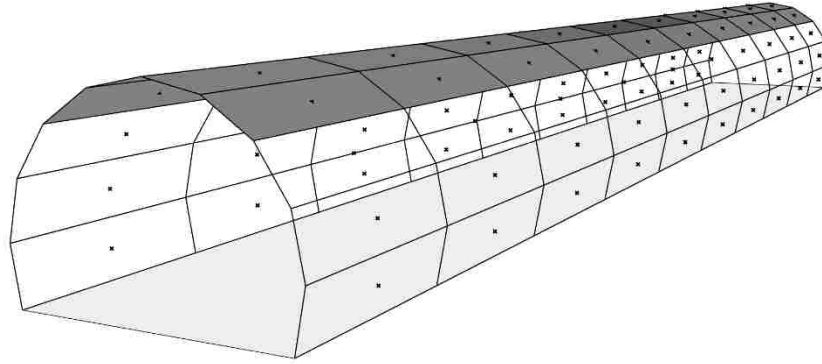
34

Figure 28 – Target elements within convective zone

Maximum convective heat flux is determined through the empirical correlation shown in Figure 9 and Equation 11.

$$q_{c,max} = 0.9778(70MW) - 26.118 = 42.3 \frac{kW}{m^2}$$

Applying the longitudinal scaling correlations detailed in Equations 12-14 to $q_{c,max}$, and again scaling linearly through the depth of the convective zone, the following spatial distribution of applied convective heat flux in *(kW/m²)* rounded to the nearest integer, on the tunnel is determined. The convective, radiation only, and sum total incident heat flux in *(kW/m²)* are shown below in Figure 29.
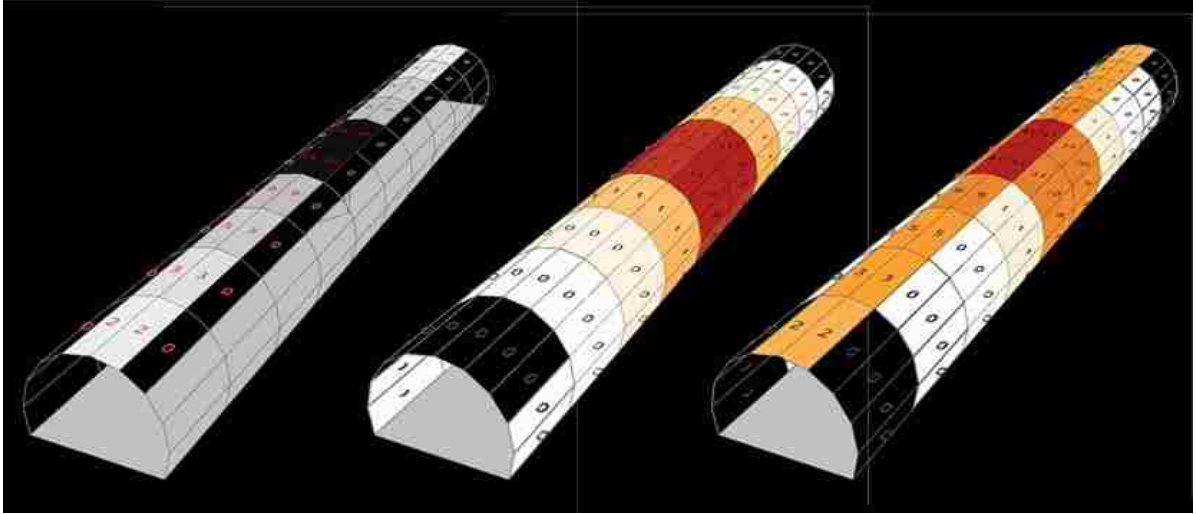
35

Figure 29 – Convective, radiative, and total incident heat flux (left to right)

COMPARISON TO FDS

To show accuracy of the current iteration of the CDSF, three fire sizes have been analyzed and compared against experimentally validated FDS solutions. The same tunnel cross section shown previously in Figure 13 is used for comparison. Tunnel wall thickness is taken as 630 *mm* per previous work done by the author in the case of tunnel blast damage utilizing the same cross section (Bai et al. 2018). The selected scenarios represent three types of vehicular fires: bus, light heavy goods vehicle (HGV) and heavy HGV with HRR of 30MW, 70MW and 200MW, respectively (Association 2011). Vehicle dimensions are selected in accordance with available design guidance AASHTO (American Association of State Highway and Transportation Officials 2001), shown in the analyzed tunnel cross section for scale, Figure 30.
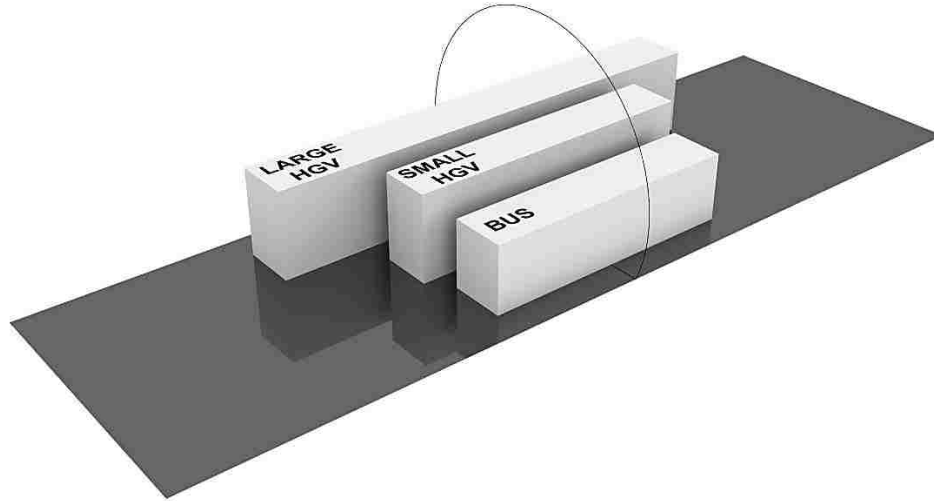
36

Figure 30 – Vehicle scenarios in tunnel cross section

Equivalent diesel footprints (solid) and vehicle footprints (dashed) are additionally shown below in Figure 31.
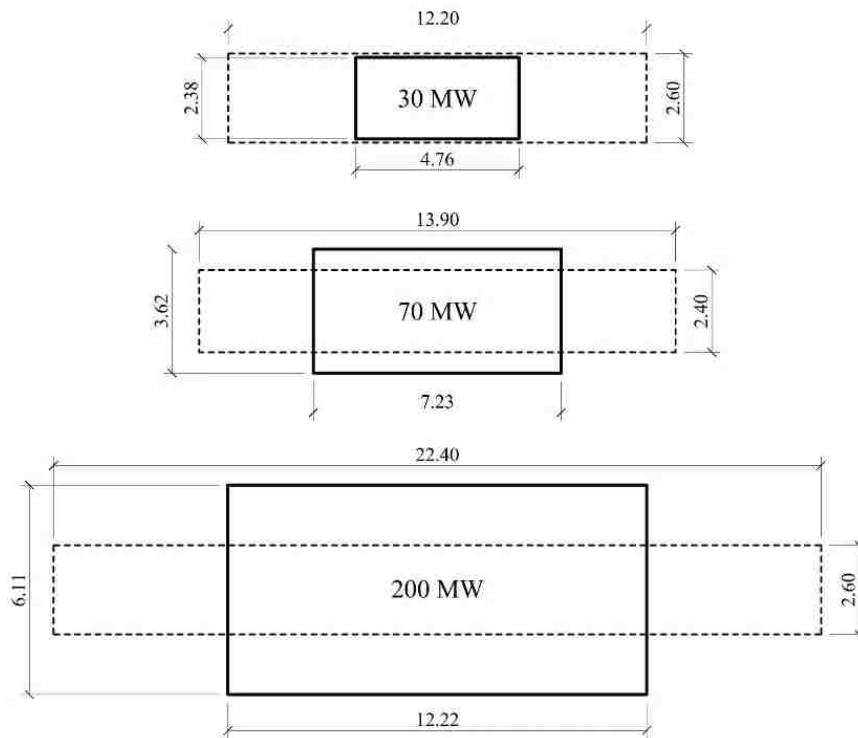

Figure 31 – Dimensioned equivalent diesel footprints (*m*)

37

Analysis carried out with the CDSF is presented at select locations along the ceiling, sidewall and cross section of the tunnel for FDS comparison, shown in Figure 32 below.
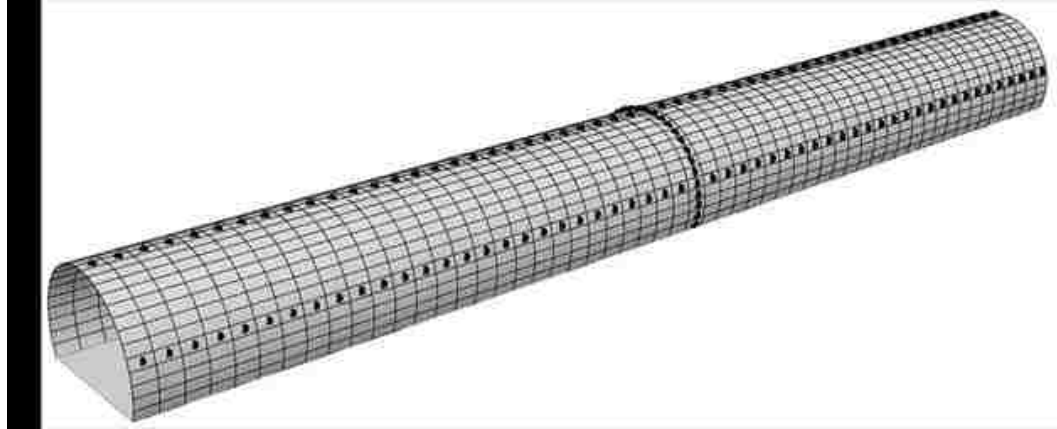

Figure 32- Measurements locations along ceiling, sidewall and cross section

While the CDSF output provides a single heat flux value at each target location, FDS provides a heat flux time history at selected measurement points. To represent the time histories generated from FDS, comparable to those from the CDSF, an upper and lower bound are determined statistically. The time history of heat fluxes (solid) shown below in Figure 33 are those directly measured at one location in the tunnel for the three selected fire sizes in FDS. The mean +/- one standard deviation is included with the time histories for the heat fluxes measured after the user-specified 30-second ramp-up threshold as the upper and lower bounds (dashed).
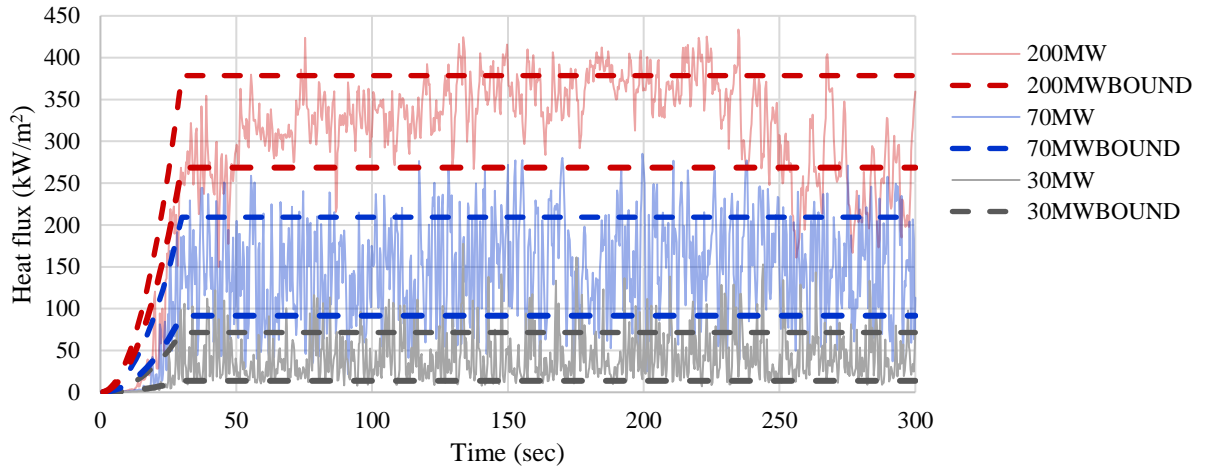
38

Figure 33 - Heat flux time history with upper and lower bounds

When considering thermal effects on humans in the event of a tunnel fire, it is appropriate to consider only peak values of thermal demands, however the case is different when evaluating thermal demands to be considered for resulting structural consequence. Through thickness temperature gradients are important in characterizing the structural response of concrete in fire for resulting damage, spalling or cracking (Le et al. 2016). Therefore, a representative analysis of thermal gradients developed from different magnitudes of heat flux is presented. Utilizing SAFIR (Franssen and Gernay 2017), a time-dependent heat flux is applied on one face of the concrete panel and temporal temperature gradients are calculated. The tunnel liner is discretized into 100 layers through its thickness to be used in the 1-D heat transfer analysis.

Ambient temperature is applied as a thermal boundary condition using the SAFIR defined F20 function. The concrete is defined as SILCONC_EN (i.e. siliceous concrete) in SAFIR, and the thermal properties are assumed according to Eurocode 2 (CEN 2004). Input parameters are summarized below in Table 3.

39

Table 3 – SILICON properties used in SAFIR

Specific mass of concrete (including moisture content)	2300 kg/m^3
Water content	45 kg/m^3
Coefficient of convection on heated surfaces	25 W/m^{2}K
Coefficient of convection on unheated surfaces	4 W/m^{2}K
Emissivity	0.8
Conductivity tuning parameter	0.5

Upper and lower bound time histories start with a 30-second t^2 ramp up to a constant heat flux are applied and remain at the constant value for the duration of analysis, illustrated above in Figure 33. The upper and lower bounds, along with FDS heat flux time history, are applied to the concrete surface for 300 seconds with a time step of one second. Comparisons of the temperature variation into the concrete liner are determined at two representative ceiling locations, (1) above fire and (2) 20 meters from fire are shown below in Figure 34, where dashed lines represent upper and lower bound flux histories and the solid lines represent the more complex FDS heat flux time history. The results are presented for the three fire cases and presented at three points in time, 50, 150 and 250 seconds.
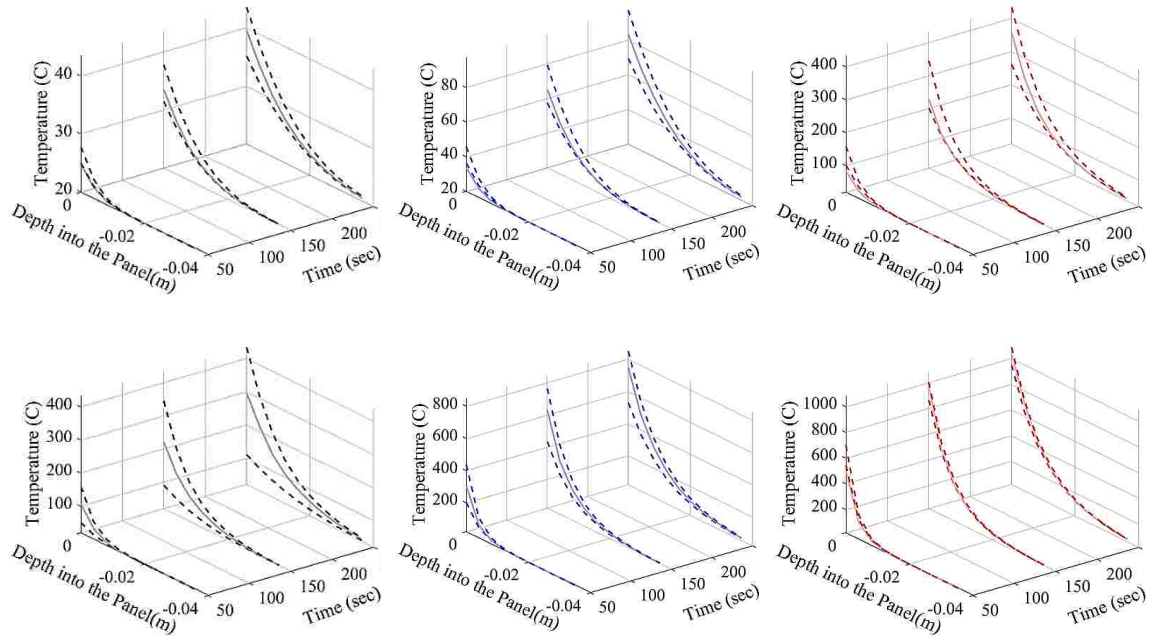
Figure 34 - Through-thickness temperature gradients above fire (top) and 20 meters from fire (bottom) for 30MW (left), 70MW (center) and 200MW (right) fires

The upper and lower bounds bracket the FDS solution of thermal gradients through the concrete section for the duration of the analysis. Subsequent FDS solutions will be presented utilizing these bounds, as they represent a holistic capture of the numerical solution. Results for the 30MW, 70MW, and 200MW with FDS upper and lower bounds, as well as the mean values from FDS after the 30 second ramp up time, are presented below in Figure 35, Figure 36, and Figure 37, respectively.
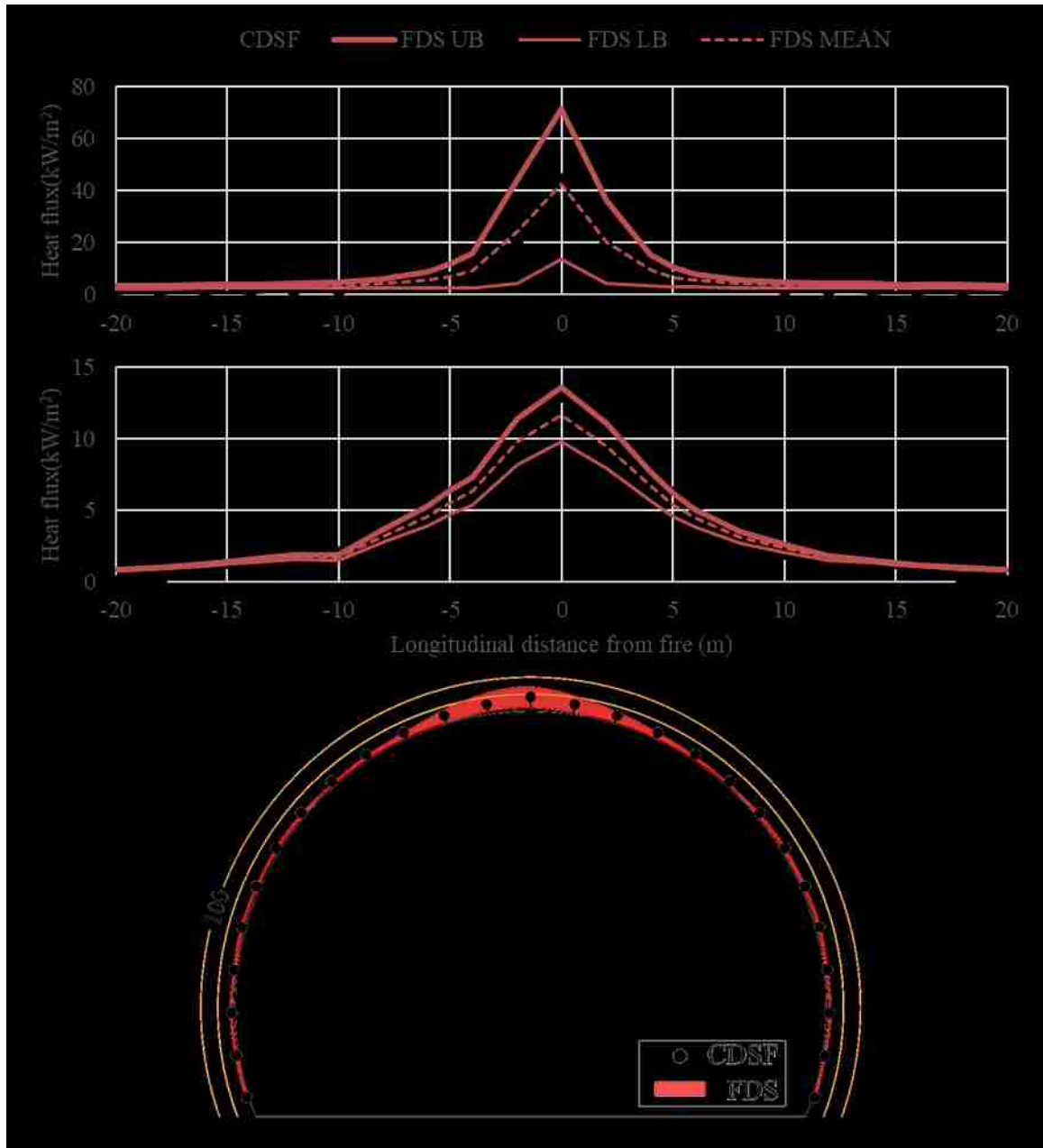
41

Figure 35 - Longitudinal (top) sidewall (center) and cross section (bottom) distribution of

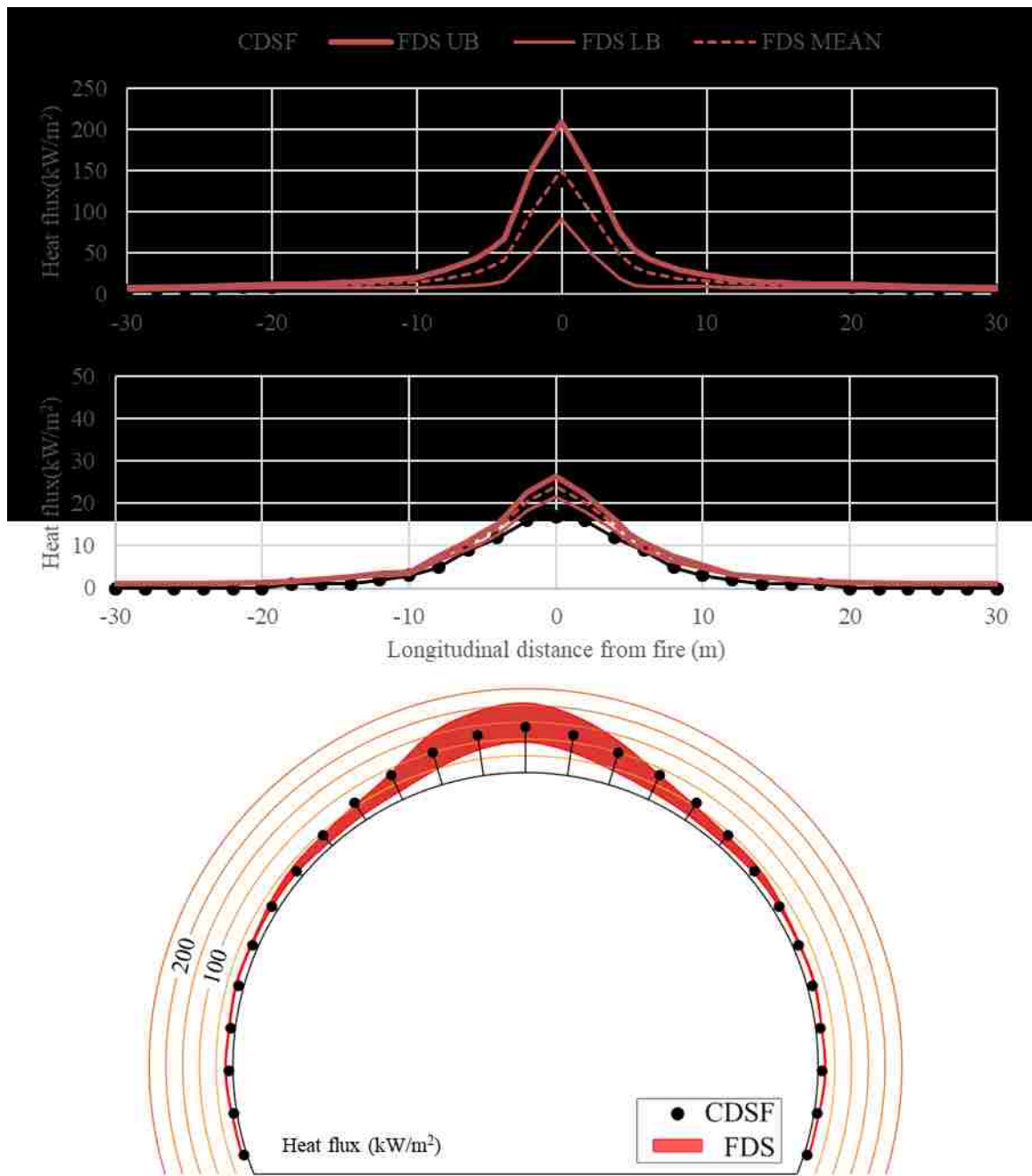incident heat flux for 30MW fire

Figure 36 - Longitudinal (top) sidewall (center) and cross section (bottom) distribution of
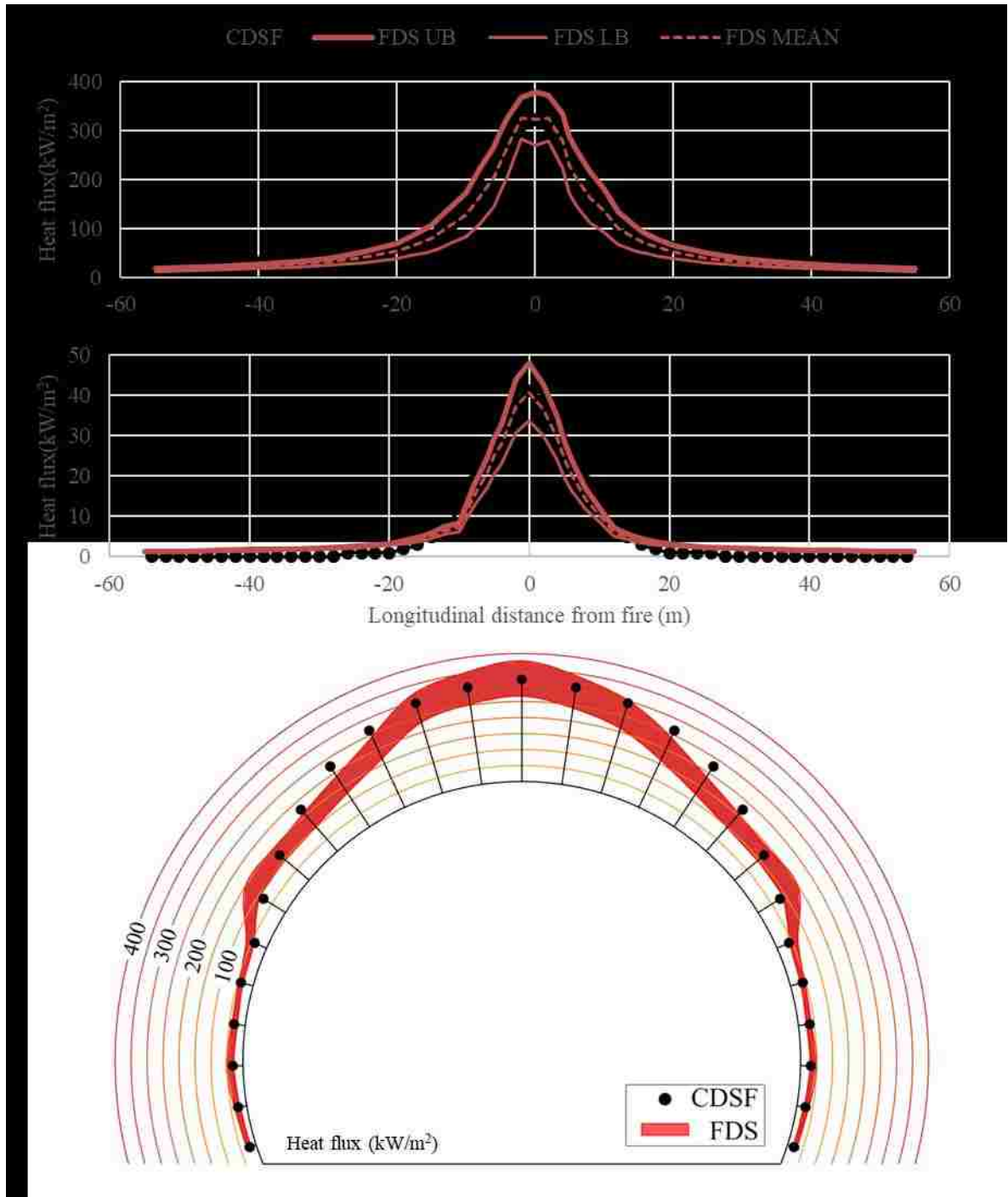
incident heat flux for 70MW fire

Figure 37 - Longitudinal (top) sidewall (center) and cross section (bottom) distribution of

incident heat flux for 200MW fire

The FDS and CDSF solutions show excellent agreement across the three fire sizes

through a broad range of incident heat fluxes. FDS solutions suggest the presence of a

44

strong ceiling jet for both the 70MW and 200MW fire, where the heat flux distribution has a discontinuity in increase through the height of the cross section. This has been accurately captured with the CDSF. Analysis time for each CDSF solution is just under 4 minutes with the current mesh discretization having a maximum edge length of no more than 85 *cm*. The computational effort required for FDS to run the 200MW fire on an equivalent desktop workstation is around 15 hours, further proving the necessity of a model which is efficient and conservatively accurate.

CONCLUSIONS

The development and verification of a confined discretized solid flame model (CDSF) has been presented. Demonstrative verification of the model with a coarse discretization has proven the architecture of the CDSF to be reliable. An evaluation of three fire sizes in a circular tunnel has proven accuracy of the model amongst a range of large scale fires. The CDSF allows for total mapping and visualization of the incident heat flux distribution on a tunnel structure, with analysis taking a fraction of the time required by computational fluid dynamics solutions.

The author notes the initially limited application of the CDSF described above, namely one tunnel shape and size. However, the framework of the model has been verified, demonstrated and can be subsequently adapted to capture a broader range of tunnel geometries. In the Grasshopper-Rhino environment, the framework is visually represented and the geometric evolution of flame shape and tunnel-flame interaction can be seen firsthand. This level of control and visual feedback allows for exciting development of complex geometry which would be near impossible with conventional programming solutions. Future work will focus on extending the range of applicability of the CDSF to

45

not only curved tunnels, but rectangular structures as well. It should also be noted that while the CDSF has been developed with tunnel application in mind, the principles and architecture of the model used can be adapted to an array of confined spaces. The author looks forward to further developing and refining the range of the CDSF, across a multitude of applications.

REFERENCES

American Association of State Highway and Transportation Officials, ed. 2001. *A Policy on Geometric Design of Highways and Streets, 2001*. 4th ed. Washington, D.C: American Association of State Highway and Transportation Officials.

Association, National Fire Protection. 2011. *NFPA 502, Standard for Road Tunnels, Bridges, and Other Limited Access Highways*. NFPA.

Babrauskas, Vytenis. 2016. "Heat Release Rates." In *SFPE Handbook of Fire Protection Engineering*, 799–904. Springer.

Bai, Fengtao, Qi Guo, Kyle Root, Clay Naito, and Spencer Quiel. 2018. "Blast Vulnerability Assessment of Road Tunnels with Reinforced Concrete Liners."

Carvel, Richard. 2004. "Fire Size in Tunnels." School of the Built Environment Division of Civil Engineering: Heriot-Watt University.

CEN. 2004. *EN 1992-1-2: Eurocode 2: Design of Concrete Structures - Part 1-2: General Rules - Structural Fire Design*.

Franssen, Jean-Marc, and Thomas Gernay. 2017. "Modeling Structures in Fire with SAFIR®: Theoretical Background and Capabilities." *Journal of Structural Fire Engineering* 8 (3): 300–323.

Hu, L. H., R. Huo, W. K. Chow, H. B. Wang, and R. X. Yang. 2004. "DECAY OF BUOYANT SMOKE LAYER TEMPERATURE ALONG THE LONGITUDINAL DIRECTION IN TUNNEL FIRES." *Journal of Applied Fire Science* 13 (1): 53–77. https://doi.org/10.2190/BQ02-N5TG-7TC7-TQFX.

Kurioka, Hitoshi, Yasushi Oka, Hiroomi Satoh, and Osami Sugawa. 2003. "Fire Properties in near Field of Square Fire Source with Longitudinal Ventilation in Tunnels." *Fire Safety Journal* 38 (4): 319–40. https://doi.org/10.1016/S0379-7112(02)00089-9.

Le, Q. X., V. T. N. Dao, C. Maluk, J. Torero, and L. Bisby. 2016. "An Investigation into Temperature Gradient Effects on Concrete Performance at Elevated Temperatures." In *The 24th Australasian Conference on the Mechanics of Structures and Materials (ACMSM24)*.

McGrattan, Kevin B, Howard R Baum, and Anthony Hamins. 2000. "Thermal Radiation from Large Pool Fires." NIST IR 6546. Gaithersburg, MD: National Institute of Standards and Technology. https://doi.org/10.6028/NIST.IR.6546.

McGrattan, Kevin B., Randall J. McDermott, Craig G. Weinschenk, and Glenn P. Forney. 2013. "Fire Dynamics Simulator, Technical Reference Guide, Sixth Edition." *Special Publication (NIST SP) - 1018*, November. http://dx.doi.org/10.1002/https:/dx.doi.org/10.6028/NIST.sp.1018.

Muñoz, Miguel, Eulàlia Planas, Fabio Ferrero, and Joaquim Casal. 2007. "Predicting the Emissive Power of Hydrocarbon Pool Fires." *Journal of Hazardous Materials* 144 (3): 725–29. https://doi.org/10.1016/j.jhazmat.2007.01.121.

National Fire Protection Association. 2016. *SFPE Handbook on Fire Protection Engineering*. 5th ed. Quincy, MA. https://doi.org/10.1007/978-1-4939-2565-0.

Quiel, Spencer E., Takayuki Yokoyama, Lynne S. Bregman, Kevin A. Mueller, and Shalva M. Marjanishvili. 2015. "A Streamlined Framework for Calculating the Response of Steel-Supported Bridges to Open-Air Tanker Truck Fires." *Fire Safety Journal*. https://doi.org/10.1016/j.firesaf.2015.03.004.

Robert McNeel & Associates. 2018a. *Grasshopper*.

Robert McNeel & Associates. 2018b. *Rhinoceros*.

Root, Kyle, Qi Guo, Spencer Quiel, and C. J. Naito. 2018. "Calculating Fire-Induced Heat Flux Contours on Concrete Tunnel Liners to Evaluate Structural Consequences." In . Belfast, UK.

Siddapureddy, Sudheer. 2013. "Characterization of Open Pool Fires and Study of Heat Transfer in Bodies Engulfed in Pool Fires." https://doi.org/10.13140/RG.2.1.5150.3841.

"The Boring Company." n.d. Accessed December 20, 2017. https://www.boringcompany.com/.

Wang, Yongdong, Alexandros Vouros, Jianping Zhang, and Michael A. Delichatsios. 2017. "Numerical and Experimental Validation Study of Flame Extent of a Pool Fire under the Ceiling." *Journal of Loss Prevention in the Process Industries* 49 (September): 652–59. https://doi.org/10.1016/j.jlp.2017.04.029.

Zhou, Kuibin, Naian Liu, Linhe Zhang, and Koyu Satoh. 2014. "Thermal Radiation from Fire Whirls: Revised Solid Flame Model." *Fire Technology* 50 (6): 1573–87. https://doi.org/10.1007/s10694-013-0360-7.
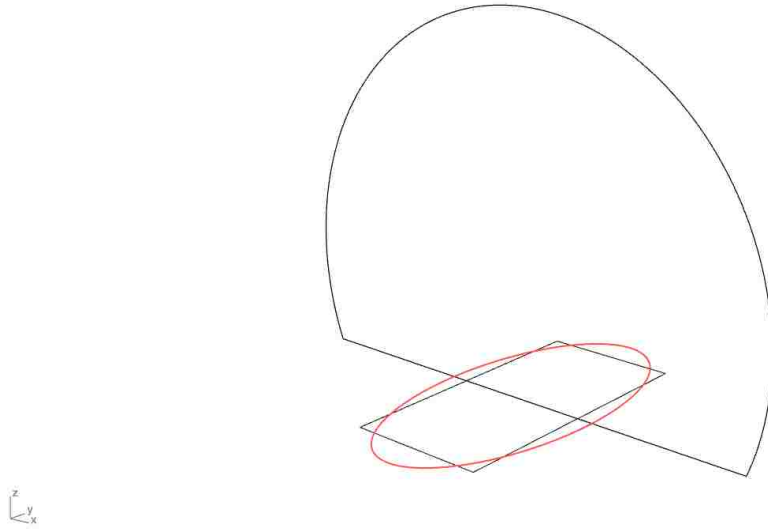
48

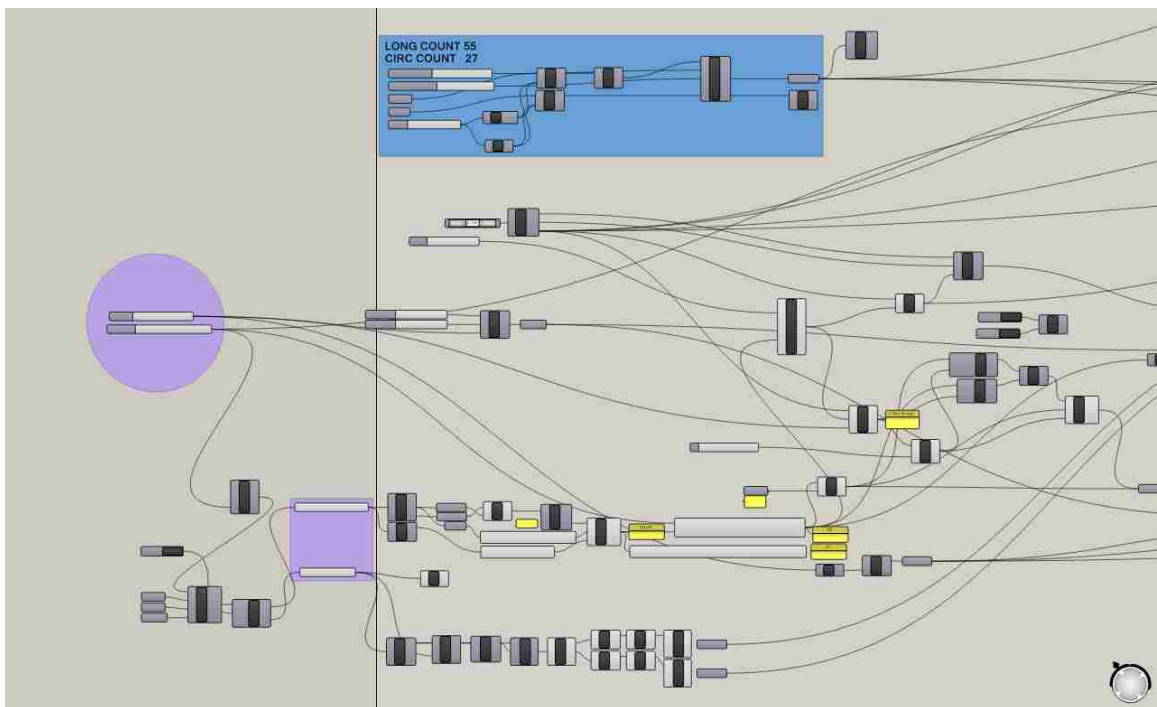# APPENDIX 1: CDSF GRASSHOPPER WORKFLOW

Figure 38 – CDSF input from Rhino
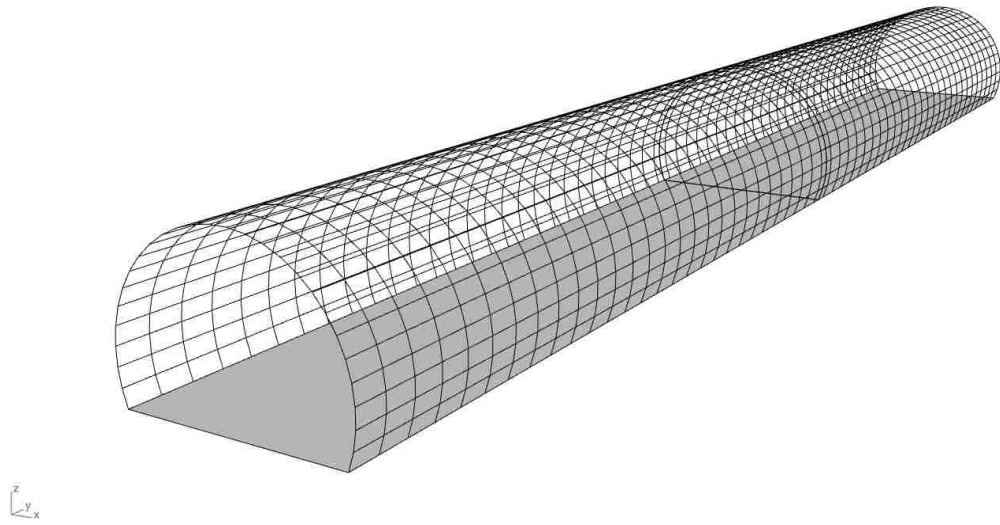

Figure 39 – CDSF workflow start in Grasshopper
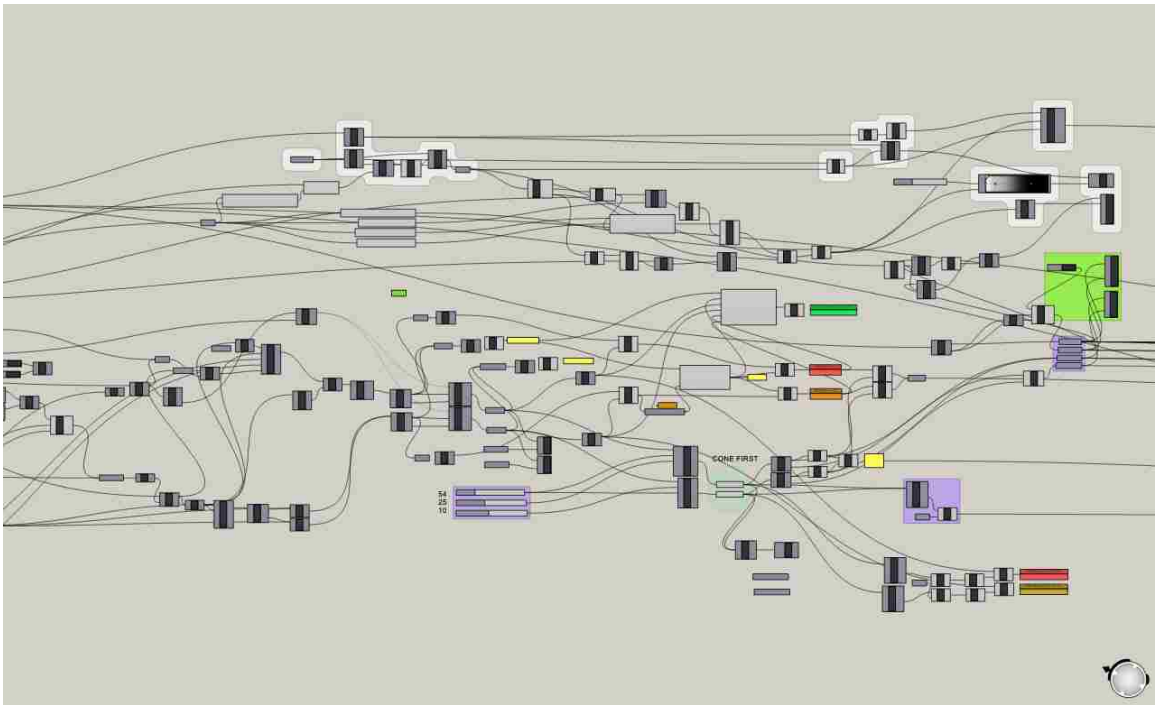
Figure 40 – Mesh creation visualized in Rhino
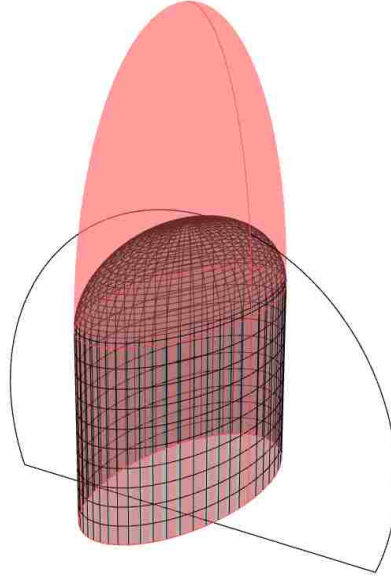

Figure 41 - CDSF workflow middle in Grasshopper

Figure 42 – Free flame and analytical flame visualized in Rhino
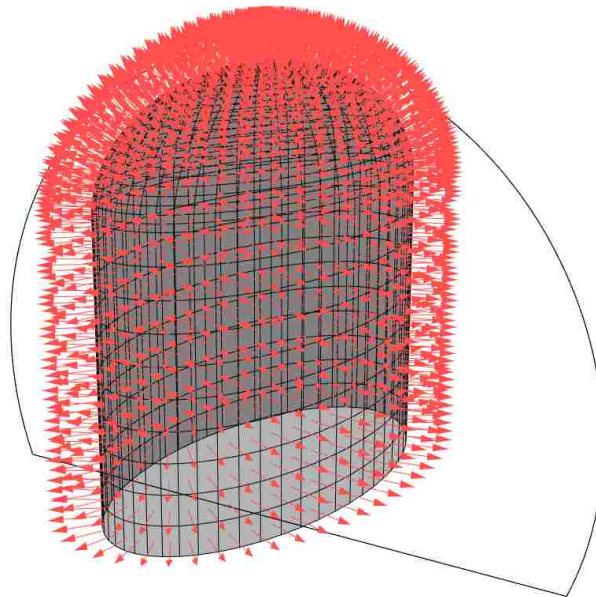
Figure 43 – Analytical flame mesh with normal vector verification visualized in Rhino
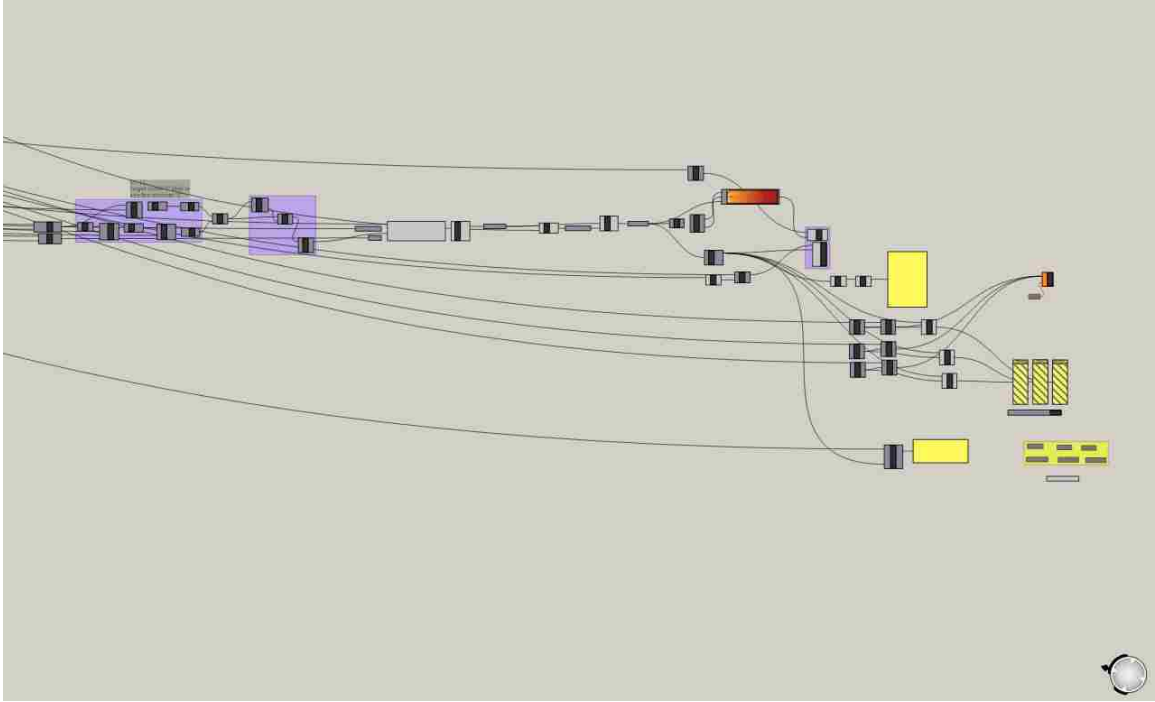
51

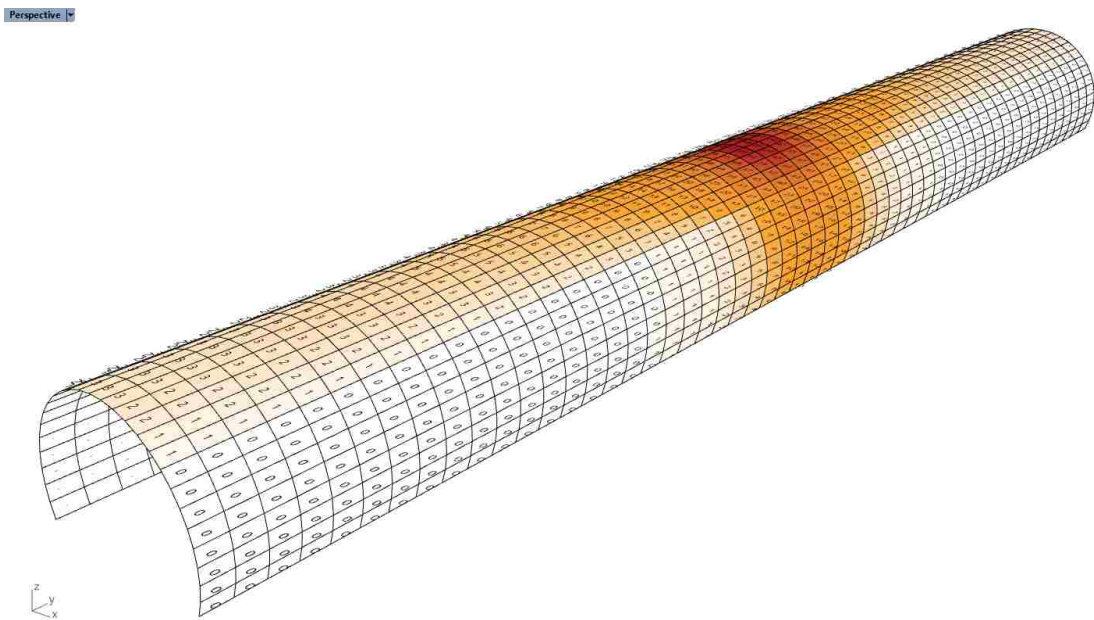Figure 44 – Final CDSF workflow stage in Grasshopper

Figure 45 – CDSF output visualized in Rhino with incident heat flux values tagged

52

VITA

Kyle Root was born in Wilmington, DE in 1994. After graduating from Concord High School in 2012, Kyle began at Lehigh University as an Integrated Civil Engineering and Architecture/Design major. He completed the integrated undergraduate degree in 2016 and continued at Lehigh University through 2017 to complete a second undergraduate degree in Civil Engineering, graduating with highest honors for both. Through his time as a Lehigh undergraduate, Kyle completed internships with Amtrak, Walt Disney World Facility Asset Management, and Thornton Tomasetti. Kyle began his graduate studies at Lehigh University in 2017 with funding provided through the Lehigh University Presidential Scholarship. Upon completion of his master's degree, Kyle will move to Philadelphia to join Thornton Tomasetti as a structural engineer.